

## Catalytic Methane Removal to Mitigate its Environmental Effect

Chao Wang, Youxun Xu & Junwang Tang\*

*Department of Chemical Engineering, University College London, London WC1E 7JE, UK*

Received (date)\*\*; accepted (date)\*\*;

Large reserve of methane, in the form of natural gas and methane hydrate, has been discovered and it has been intensively used as a fuel, or as a building block for chemical synthesis. However, severe environmental and climatic issues caused by the leakage of methane during the production, transportation and use of methane are overlooked. This offers incentives for the catalytic removal of methane. Nevertheless, due to the inert nature of methane molecules, the activation of methane via thermocatalysis requires harsh reaction conditions. The high reaction temperature not only increases the capital cost but also accelerates the deactivation of catalysts due to sintering and/or coking. The development of robust and stable catalysts with a low operating temperature has become the focus of research on thermocatalytic methane oxidation. Photocatalysis, which uses the energy of photons instead of heat to drive chemical reactions under ambient conditions, offers another approach for methane removal. This review will cover the development of high-efficiency catalysts for methane combustion in both thermo- and photo-catalysis. Moreover, the fundamental understanding of the active sites, surface chemistry and reaction pathway will also be discussed. Finally, the challenges facing in the catalytic removal of methane will be summarised and potential solutions will be provided. This review will be of interest to researchers in the field of heterogeneous catalysis, materials design, and chemical engineering.

**Methane Oxidation, Environmental Remediation, Thermocatalysis, Photocatalysis, Fundamental Understandings**

### 1 Introduction

#### 1.1 Background

Methane with a huge reserve is a strong greenhouse gas with a global warming potential nearly 30 times higher than CO<sub>2</sub>. It can be emitted into the atmosphere via various pathways, such as farming, decay of waste landfills, and most importantly the exploitation, production, transportation and consumption of natural gas, coal and oil. The increase of methane concentration in the atmosphere equals 25 million tons of methane emission each year after 2006. Thus, controlling or reducing the amount of methane in the atmosphere could contribute significantly to mitigating its

climate effect.

The atmospheric methane removal processes occur naturally in the atmosphere and soil. In the atmosphere, methane reacts with the free hydroxyl or chlorine radicals to produce methyl radicals and water or HCl. Under the assistance of O<sub>2</sub> and NO, the oxidation process eventually leads to the production of formaldehyde and water vapour. The whole process results in an estimated methane lifetime of 10 years [1]. In soil, methane is destroyed by methanotrophic bacteria to release carbon dioxide and water in methane-rich areas.

Artificial methane removal is attempted via physical, biological, and chemical pathways. Physically, iron-salt aerosols were proposed to remove methane in the lower troposphere by enhancing the concentration of OH· and chlorine

\*Corresponding authors (email: junwang.tang@ucl.ac.uk)

radicals through the Fenton and photo-Fenton reactions [2]. Considering the cost of aerosols and the risk of detrimental effects on the respiration of animals and people caused by the existence of aerosols in the atmosphere, this method can only be applied on a small scale and in remote areas. Biologically, modification of the activity of microbes via soil amendments or applying biotrickling filters, has contributed to lowering the methane concentration in the atmosphere [3,4]. However, the atmospheric concentration of methane is too lean for bacteria survival. Thus, relatively high methane concentration and a certain temperature are required for the functional operation of such biological processes. Chemically, methane can be oxidised through thermo- or photocatalytic processes. Compared with the physical and biological methods, catalytic processes realise continuous and rapid methane removal under certain reaction conditions. Gas mixtures containing either high or low levels of methane could be selectively converted to carbon dioxide. The cost is relatively controllable through the development of inexpensive catalysts and reactor engineering. Furthermore, the catalytic methane oxidation process causes minimum harmful effects on the environment. Finally, catalytic methane oxidation could be applied in automobile engines or other methane-consuming setups to avoid methane emission and mitigate the environmental issue. Therefore, catalytic methane oxidation is an ideal pathway for methane removal.

To achieve in situ removal of methane to reduce its emission, the catalytic methane oxidation can be directly applied in venues including ventilation of coalmines/gas fields, exhausts of power plants, automobiles, and home fireplaces and boilers. Considering the concentration of atmospheric methane is too low for direct conversion, various technologies can be used to enrich methane from low concentrations. For example, a two-stage methane enrichment process with initial vacuum, temperature, and final vacuum swing adsorption was designed [5]. Via this methane enrichment unit, air streams with methane of 0.3% and 1.0% were enriched to 19% and 37%, respectively. Moreover, gas separation membranes and other technologies such as mechanical towers and vortex tubes were used to enrich the methane concentration mechanically [6,7]. Porous materials such as metal organic frameworks [8], covalent organic frameworks [9], and zeolites [10], with high methane storage capacities, were also designed that can be potentially combined with methane oxidation catalysts to achieve atmospheric methane removal. Therefore, the removal of methane via catalytic oxidation holds both great importance in research and significant potential for large-scale applications.

Thermocatalytic methane oxidation has been studied since 1927 [11]. With the effort of nearly one century, Pd-based materials were proved to be the most efficient catalysts [12–14]. Some transition metal oxides (e.g.,  $\text{Co}_3\text{O}_4$  and perovskites) were also used as methane oxidation catalysts [15–17], due to economic considerations, although

demonstrating moderate performance compared with Pd-based catalysts. Normally, the complete oxidation of methane by thermocatalysis requires high reaction temperatures (e.g.,  $> 400\text{ }^\circ\text{C}$ ). The operation condition requires the catalyst to be heat resistant. More importantly, the high temperatures promote the formation of  $\text{NO}_x$  and other substances that are detrimental to the environment, and/or poison the catalysts. Therefore, it is essential to develop robust and sintering-resistant catalysts for methane oxidation that work under lower temperatures.

Low-temperature catalytic processes, such as photocatalysis, electrocatalysis, photoelectrocatalysis have been developed to drive reactions under mild conditions, replacing high temperatures required by traditional thermocatalysis, such as ammonium synthesis from  $\text{N}_2$  reduction, hydrogen evolution from water splitting, and hydrocarbons/oxygenates production from carbon dioxide hydrogenation [18–20]. Since methane oxidation is a gas phase reaction, and the solubility of methane in most electrolytes is extremely low, only photocatalysis has been proved efficient for methane conversion at low temperatures [21–24]. The development of methane oxidation photocatalysts is at an infant stage. Up to now,  $\text{TiO}_2$  and  $\text{ZnO}$  are the most used photocatalysts for the oxidation of methane [25–28]. Besides,  $\text{SrTiO}_3$  and  $\text{AgCl}$  were also reported as photocatalysts for the total oxidation of methane [29,30]. The performance of methane oxidation by photocatalysis is relatively low compared with thermocatalysis. Nonetheless, photocatalytic methane oxidation has shown its potential as a low-temperature technology for methane oxidation.

## 1.2 Preliminary mechanism of thermocatalysis and photocatalysis

Complete oxidation of methane to  $\text{CO}_2$  ( $\text{CH}_4 + 2\text{O}_2 \rightarrow \text{CO}_2 + 2\text{H}_2\text{O}$   $\Delta G = -800.9\text{ kJ/mol}$ ) is a thermodynamically favourable exothermic reaction. However, the inert nature and high energy of the first C-H bond in methane (439 kJ/mol) limits the kinetics of the methane oxidation reaction. Thus, activation of the C-H bond in methane is considered the rate-limiting step in methane oxidation [31]. After breaking the first C-H bond, a methyl radical ( $\cdot\text{CH}_3$ ) is formed, which is the first and most important intermediate in all methane conversion processes. Afterwards,  $\cdot\text{CH}_3$  is further oxidised via a series of radical reactions, finally resulting in the formation of  $\text{CO}_2$ .

In thermocatalytic methane oxidation, methane activation in the presence of a catalyst follows a dissociative adsorption process, as shown in Figure 1a [32]. Methane molecules are firstly adsorbed on the active site of a catalyst. With the input of heat energy and the assistance of the catalytic active species, the breaking of the first C-H bond results in the formation of a methyl radical and hydrogen radical. Then, the formed methyl radical is either oxidised by the reactive oxygen species (ROS) formed by oxygen acti-

vation or undergoes further dehydrogenation followed by a completed oxidation process by ROS. A light-off curve, which shows the relationship between methane conversion and the reaction temperature, is used to evaluate the performance of a methane oxidation catalyst (Figure 1b) [33]. As the temperature increases, the oxidation process is initiated at a temperature related to the intrinsic properties of the catalyst (stage 1). An exponential increase in methane conversion is observed with a further increase in the reaction temperature (stage 2), at which point, the heat generated by the oxidation reaction is greater than the heat supplied by the reaction chamber. Then, the reaction rate increases rapidly with the temperature (stage 3). At this stage, the reaction is mainly controlled by mass transfer. Finally, the conversion gradually reaches 100% as the reactants are depleted (stage 4). The “light-off” point can be defined in various ways, however, all of which are referred to as the point when mass transfer becomes rate-controlling [33]. The light-off point is defined as the temperature when methane conversion reaches 10%, 20% or 50%. However, due to the shape of the curve, there is very little difference in the temperature between different definitions. The kinetics of the reaction is reflected in stage 1 and 2, while stage 3 and 4 are mainly affected by the geometry of the catalyst (e.g., surface area and porosity) and the structure of the reactors. It is ideal to completely convert methane into carbon dioxide and water (100% methane conversion) in real applications. Therefore, high reaction temperatures ( $> 400$  °C) cannot be avoided. For supported catalysts, the mobility of nanoparticles on the support significantly increases at elevated temperatures, which causes aggregation and deactivation of the catalyst. Therefore, catalyst stability is another important concern.

In photocatalysis, light energy is the main energy input to drive chemical reactions in the presence of a photocatalyst. Most photocatalysts are semiconductor-based materials. In a typical photocatalytic process (Figure 1c), the electrons at the valence band (VB) of a semiconductor are populated to the conduction band (CB) upon light irradiation, leaving holes at the VB (Step ①). Then, the electrons and holes transfer from the bulk to the surface of the catalyst (Step ②). In the meantime, recombination of charges can occur, which results in decreased photon efficiency (Step ③). The electrons and holes at the surface finally react with the reactants in reduction (Step ④) and oxidation (Step ⑤) reactions, respectively. In thermocatalysis, all energy required to overcome the activation barrier is supplied by external heat (Figure 1d). Thus, high temperatures are required. However, the energy source in photocatalysis is photons, instead of heat. Only moderate heat energy is required with the aid of photons. Hence, compared with thermocatalysis, the activation energy and reaction temperature of photocatalytic processes can be significantly reduced [34]. In photocatalytic methane oxidation, the oxidative holes are considered to be responsible for breaking the first C-H bond in methane. Ac-

tivation of methane by energetic holes results in the formation of methyl radicals ( $\cdot\text{CH}_3$ ) and protons. Subsequently, complex radical reactions occur. The most accepted theory is that  $\cdot\text{CH}_3$  is firstly oxidised to HCHO as an intermediate. Then, HCHO undergoes further oxidation following the order of to HCOOH and finally to  $\text{CO}_2$  and  $\text{H}_2\text{O}$ . An ideal methane oxidation photocatalyst should exhibit a strong light absorption capability, low charge recombination rate, suitable band potential for both methane oxidation and oxygen reduction, and high stability against photo-corrosion. Moreover, considerations in thermocatalysis such as strong interaction between the catalyst surface and reactants as well as the fast desorption of products should also be applied in the development of photocatalysts.

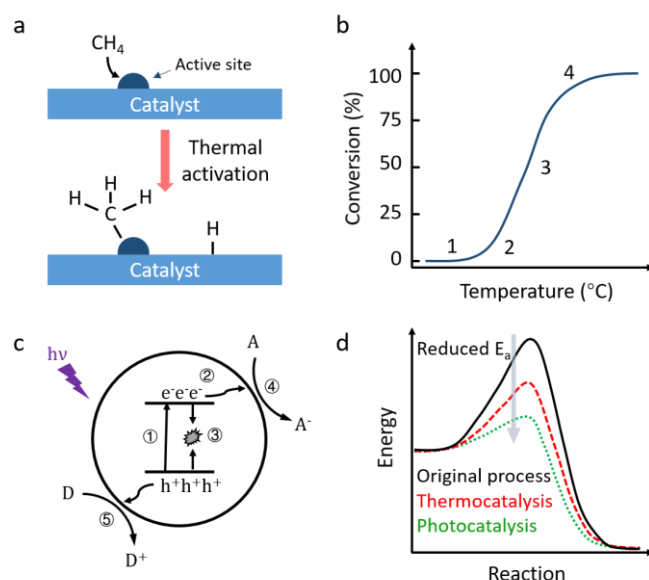


**Figure 1.** (a) Dissociative adsorption of methane via thermocatalysis; Reprinted from ref. [32]. Copyright 2022 American Chemical Society (colour online). (b) Light-off curve for thermocatalytic methane oxidation; Reprinted from ref.[33]. Copyright 1995 Elsevier (colour online). (c) A schematic diagram of a typical photocatalytic process; (d) Energy diagram showing the methane oxidation process via photocatalysis and thermocatalysis. Reprinted from ref. [34]. Copyright 2022 Springer Nature (colour online).

### 1.3 Practical conditions of catalytic methane oxidation

In most studies, dry methane and pure  $\text{O}_2$  are applied, sometimes with Ar as the balance gas in the catalytic oxidation of methane. Limited discussion concerning specific application conditions for catalytic combustion of methane is addressed although catalytic methane combustion has been studied for nearly a century. A few important practical aspects necessitate further detailed investigation, such as the reactivity and stability of the catalyst under humid conditions and other compounds. For instance, the exhaust gas going through the catalytic converters of natural gas vehicles contains low concentrations of methane ( $\sim 1000$  ppm), large amounts of  $\text{H}_2\text{O}$  (10–15%) and  $\text{CO}_2$  (15%), as well as

CO, NO<sub>x</sub> and sulfuric compounds. H<sub>2</sub>O could promote the sintering of noble-metal-based catalysts under high temperatures. CO, NO<sub>x</sub> and sulfuric compounds could be preferentially adsorbed on the active sites, therefore poisoning the catalyst. In coal ventilation air, humid and coal dust may also affect the catalytic activity and stability. It has been reported that the performance of the catalytic systems dropped dramatically in the presence of water vapour [35]. Especially in photocatalytic methane oxidation, attention should be paid to simulating the practical operation conditions when evaluating the catalyst performance. In the test of photocatalytic methane oxidation, diluted methane (100 ppm) in the presence of a high concentration of pure O<sub>2</sub> is normally used to obtain a noticeable methane conversion rate, not to mention the long reaction time. Moreover, batch reactors are frequently used in photocatalytic methane oxidation. This is not desirable, as continuous conversion is required in actual application scenarios [36].

## 2 Thermocatalytic methane combustion

The first study of thermocatalytic methane oxidation can be dated back to 1927 [11]. A series of transition metal oxides were compared and Co<sub>3</sub>O<sub>4</sub> was found to be the most efficient. Afterwards, Pd and other noble metals were developed as active catalysts for methane oxidation [37]. In particular, Pd has been intensively studied. The effects of the size, morphology and chemical states of Pd, and different supports on the performance were investigated [37,38]. In this section, the recent progress in the state-of-the-art catalysts for thermocatalytic combustion of methane will be introduced. Noble-metal-based catalysts will be given extra focus due to their high performance and stability. Noble-metal-free catalysts will also be discussed. Catalyst deactivation caused by high temperature, humid, SO<sub>2</sub>, etc. will be discussed. Finally, the fundamental studies on thermocatalytic methane oxidation using advanced spectroscopies and microscopies will be summarised.

### 2.1 Catalyst development

Noble metals and non-noble metal oxides are used as catalysts for methane oxidation. Noble metals, including Pd, Pt, etc. show higher performance than metal-oxide-based catalysts [39]. The drawbacks of noble metal catalysts are high cost and poor stability at elevated reaction temperatures [40]. Metal oxides (e.g., CeO<sub>2</sub>, Co<sub>3</sub>O<sub>4</sub>, and perovskites) were also studied for methane combustion. Metal oxides, although displaying moderate catalytic efficiency and relatively high light-off temperatures, are more attractive methane oxidation catalysts due to economic considerations.

#### 2.1.1 Noble-metal-based catalysts

Pd is the most widely used noble metal as methane oxidation catalyst. Other precious metals, such as Pt, Rh, Ir, Au

and Ru also demonstrated excellent performance for methane oxidation [41–44]. Noble metals can be used directly or with a support. However, supported catalysts show higher activities due to a high dispersity of metals and the interaction between metals and the supports. Frequently used supports include Al<sub>2</sub>O<sub>3</sub>, CeO<sub>2</sub>, ZrO<sub>2</sub> and zeolites. The size and chemical states of noble metals [45–47], as well as the interaction with the support [48–51], all have a significant effect on the catalytic activity. Moreover, the poisoning and deactivation of the catalysts [52] and strategies to avoid such behaviours will be covered.

Pd-based catalysts are very active in the complete oxidation of methane. Therefore, intensive attention has been paid to Pd catalysts in the past decades. Up to now, the temperature for 50% conversion of methane achieved over Pd-based catalysts can be as low as 200 to 300 °C [53]. Two active states are usually observed in the catalytic combustion of methane, namely Pd and PdO [54,55]. The two phases may co-exist in the catalyst, and the transition between Pd and PdO may occur during the catalytic reaction. PdO is commonly accepted as a more active state than Pd. It was observed that PdO decomposed into metallic Pd at elevated temperatures and was re-oxidised into PdO upon cooling [56].

The support of Pd can have a significant effect on the performance of the catalysts due to the strong metal-support interaction. Metal oxides, such as CeO<sub>2</sub>, TiO<sub>2</sub>, Al<sub>2</sub>O<sub>3</sub> and ZrO<sub>2</sub>, are an important group of materials used as the supports for Pd species [12,57–62]. Pd was loaded on CeO<sub>2</sub> by a deposition-precipitation method (Pd-DP) [63]. It was found that Pd-DP displayed significantly improved methane oxidation performance compared with the same catalysts prepared by the impregnation method (Pd-IM) or Pd supported on Al<sub>2</sub>O<sub>3</sub> (Pd-A) by the deposition-precipitation method. The temperature for 50% methane conversion achieved over Pd-DP was as low as 257 °C, which was much lower than that of Pd-IM at 557 °C and Pd-A at 349 °C. It was claimed that the high oxygen mobility of Pd-DP guaranteed that PdO<sub>x</sub> could not be reduced to the metallic state. Therefore, the high activity was ascribed to the low reducibility of Pd species on Pd-DP relative to that on Pd-IM and Pd-A, as proved by the X-ray photoelectron spectroscopy (XPS) analysis of the Pd species. Al<sub>2</sub>O<sub>3</sub> is another common support owing to its excellent thermal stability, high surface area and mechanical strength. Pd particles of various sizes were loaded on  $\alpha$ -Al<sub>2</sub>O<sub>3</sub>,  $\theta$ -Al<sub>2</sub>O<sub>3</sub> and  $\gamma$ -Al<sub>2</sub>O<sub>3</sub>, respectively [12]. The catalytic activity of Pd- $\alpha$ -Al<sub>2</sub>O<sub>3</sub> and Pd- $\theta$ -Al<sub>2</sub>O<sub>3</sub> showed a volcano-shaped dependence on the size of Pd particles, while that of Pd- $\gamma$ -Al<sub>2</sub>O<sub>3</sub> increased with the particle size (Figure 2a). The authors used <sup>27</sup>Al MAS-NMR to detect the fraction of pentacoordinate Al<sup>3+</sup> sites in the supports, which was the origin of the metal support interaction. A strong metal-support interaction was observed over Pd- $\gamma$ -Al<sub>2</sub>O<sub>3</sub>, while the inter-

action was moderate in  $\alpha$ - and  $\theta$ - $\text{Al}_2\text{O}_3$  loaded with Pd. The weak metal-support interaction in Pd- $\alpha$ - $\text{Al}_2\text{O}_3$  and Pd- $\theta$ - $\text{Al}_2\text{O}_3$  encouraged the formation of spherical or well-faceted Pd particles. The strong interaction in Pd- $\gamma$ - $\text{Al}_2\text{O}_3$  caused distorted Pd particles. With the assistance of the infrared (IR) spectra of CO-adsorption and transmittance electron microscopy (TEM) analysis of the catalysts, it was found that step sites on Pd particle surface were the main cause for the methane oxidation (Figure 2b). The activity of the Pd surface sites followed the order of step > plane > corner  $\approx$  single atoms.

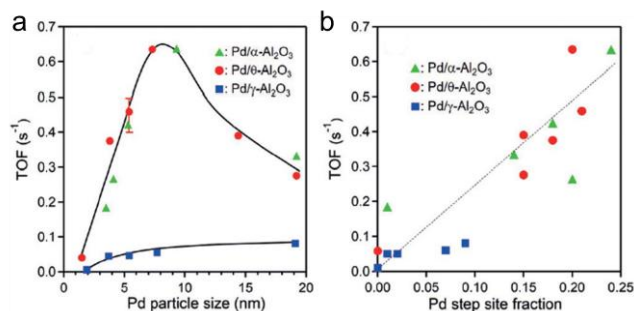


**Figure 2.** (a) Dependence of the turnover frequency (TOF) at 300 °C for methane oxidation on Pd particle size; (b) Plot of TOFs at 300 °C for methane oxidation against the fraction of step sites. Reprinted from ref. [12]. Copyright 2017 John Wiley and Sons Ltd. (colour online).

Zeolites have been widely used as promising supports because of their well-defined channels, high surface area and excellent thermal stability [64,65]. The most important advantage of using zeolites as the support is its ability to constrain the metal nanoparticles and reduce the sintering of catalysts. Pd was loaded on mordenite zeolite (Pd/H-MOR) by the ion-exchange method [66]. It was reported that increased acidity of zeolites could enhance the mobility of palladium over the support under reaction conditions, which resulted in particle growth and catalyst deactivation [67]. Thus, the acid sites of Pd/H-MOR were exchanged by sodium through sodium bicarbonate titrating to obtain Pd/Na-MOR. The temperature for 50% methane conversion was reduced from 400 °C to 340 °C. Moreover, Pd/Na-MOR showed excellent hydrothermal resistance (Figure 3a). STEM images of catalysts after long-term reaction showed no significant change in the dispersion of Pd species in Pd/Na-MOR, while sintering of the active phase in Pd/H-MOR was observed. The in-situ X-ray absorption spectroscopy for catalysts ageing indicated the fraction of Pd-Pd coordination increased in Pd/H-MOR but Pd-O was the dominant component in Pd/Na-MOR after treatment at 410 °C in the presence of 5% water. Another interesting result was that the catalysts showed improved performance after a pulse reduction by removing oxygen in the atmosphere (Figure 3b). Pd<sup>2+</sup> species were reduced immediately in the absence of oxygen, accompanied by decreased me-

thane conversion. When oxygen was re-introduced, Pd was gradually oxidised back to Pd<sup>2+</sup>, and higher performance of the catalysts than before reduction was obtained. The improved methane conversion was ascribed to the formation of highly dispersed PdO phase by redispersion, increased surface roughness of freshly reoxidised PdO, or the interaction between the reduced and oxidised Pd. Via the pulse reduction-reoxidation technique, the Pd/Na-MOR displayed a high methane oxidation performance without deactivation for over 90 h in the presence of steam (Figure 3c). Very recently, Pd was confined in single crystalline silicalite-1 (S-1) zeolite with intra-mesopores for light alkanes oxidation [53]. The pore size in traditional zeolites was  $\sim$ 2 nm, which limited the molecular diffuse. With the introduction of mesopores in S-1, the mass transfer was significantly improved. More importantly, Pd nanoparticles were encapsulated in the zeolite instead of loaded on the surface, which realised stable methane oxidation with a 50% methane conversion temperature of 261 °C.

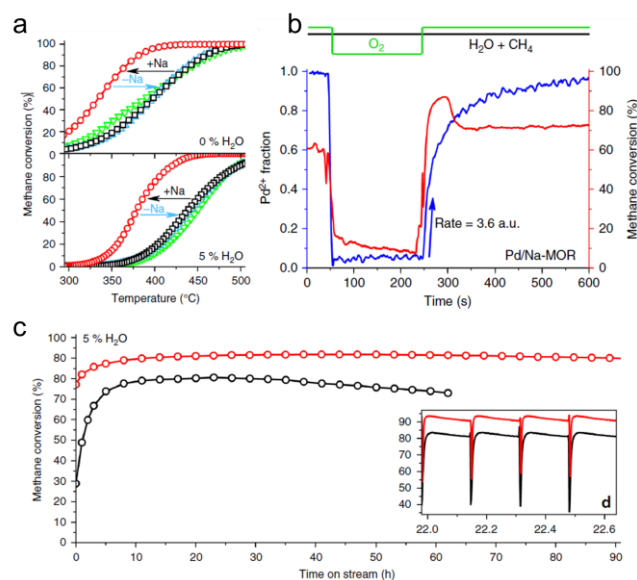


**Figure 3.** (a) Light-off curves for methane oxidation with and without 5% water; (b) Fraction of oxidized palladium in Pd/Na-MOR and corresponding catalytic activity; (c) Stability test with continuous short pulse regeneration, insert (d) shows the magnification of four cycles with regeneration. Reprinted from ref. [66]. Copyright 2018 Springer Nature (colour online).

Pd was also loaded on some mixed oxides, such as MgAl<sub>2</sub>O<sub>4</sub>, NiCo<sub>2</sub>O<sub>4</sub>, Al<sub>2</sub>O<sub>3</sub>-CeO<sub>2</sub>, etc [68–70]. The mixed oxide is believed to combine the advantages of two oxides, therefore improving the hydrothermal resistance, long-term stability and/or catalyst activity. Pd loaded on Ce<sub>x</sub>Zr<sub>1-x</sub>O<sub>2</sub>-Al<sub>2</sub>O<sub>3</sub> displayed a 99% methane conversion at the temperature of 455 °C, which was much lower than that of Pd-Al<sub>2</sub>O<sub>3</sub> (485 °C) [71]. With further Mg-doping in the support, the temperature was reduced to as low as 400 °C at 1 vol% CH<sub>4</sub> and 5.0 vol% O<sub>2</sub> in N<sub>2</sub> as balance gas with a

GHSV of 50 000 mL h<sup>-1</sup> g<sup>-1</sup>. Doping of Mg into the lattice of Ce<sub>x</sub>Zr<sub>1-x</sub>O<sub>2</sub>-Al<sub>2</sub>O<sub>3</sub> induced oxygen vacancies and favoured oxygen migration, which resulted in a smooth transformation between Pd and PdO and was beneficial for methane oxidation.

To further improve the stability and sintering resistance, a second component is introduced into the Pd-based catalysts. Bi-metallic methane combustion catalysts consisting of Pd with another noble metal (Pt, Au, Ir, Rh, Ag,) or transition metal (Ce, Co, Ni, Cu) are attracting increasing attention in the catalytic methane oxidation reaction [72–74]. Among noble metals, Pd-Pt bi-metal catalysts are the most effective, stable and resistant combination [75,76]. A recent report demonstrated the formation of 2-D PdO<sub>x</sub> rafts on Pt single atoms anchored CeO<sub>2</sub> catalyst (1Pd/2Pt@CeO<sub>2</sub>) [76]. It was found that after Pt single atoms were trapped at the step-sites of CeO<sub>2</sub>, further loading of noble metals (e.g., Pt and Pd) results in the formation of 2-D rafts instead of 3-D nanoparticles (Figure 4a). Compared with the reference catalyst (denoted as (1Pd+2Pt)/CeO<sub>2</sub>) with the same metal loading but prepared by the conventional impregnation and calcination method, 1Pd/2Pt@CeO<sub>2</sub> displayed significantly improved water-resistant activity. The methane conversion loss of 1Pd/2Pt@CeO<sub>2</sub> in the presence of 4% and 10% water vapour were 3.8% and 15.7%, much lower than that of (1Pd+2Pt)/CeO<sub>2</sub> (23.2% and 44.3% performance loss). Both catalysts were stable and could catalyse methane oxidation in a period of 12 h in the presence of 4% water vapour, though 1Pd/2Pt@CeO<sub>2</sub> displayed higher activity (Figure 4b). According to DFT calculations, the enhanced methane conversion activity of 1Pd/2Pt@CeO<sub>2</sub> was ascribed to the decreased energy barrier for methane activation. The superior water resistance was due to the high dissociation energy of water on the 1Pd/2Pt@CeO<sub>2</sub> surface. This minimised the amount of OH radicals strongly adsorbed at the catalyst surface, which is the main cause of catalyst deactivation. To modify the performance of methane combustion and minimise the deactivation of catalysts, a Pd@CeO<sub>2</sub> core-shell supramolecular structure was loaded on a special hydrophobic Al<sub>2</sub>O<sub>3</sub> support [77]. Over the optimised catalysts (Pd@CeO<sub>2</sub>/H-Al<sub>2</sub>O<sub>3</sub>), complete conversion of CH<sub>4</sub> was observed when using a gas stream of 0.5 volume % CH<sub>4</sub> and 2.0 volume % O<sub>2</sub> in Ar at a space velocity of 200 000 ml g<sup>-1</sup> h<sup>-1</sup> at ~ 400 °C (see Figure 4c). The reaction rate of Pd@CeO<sub>2</sub>/H-Al<sub>2</sub>O<sub>3</sub> was much higher than the reference catalysts with a similar methane activation energy, as shown in Figure 4d. The high performance of the Pd@CeO<sub>2</sub>/H-Al<sub>2</sub>O<sub>3</sub> was ascribed to the strong interaction between Pd and CeO<sub>2</sub>. More importantly, The Pd@CeO<sub>2</sub> structures remained isolated even after the reaction at 850 °C. The transformation of Pd to PdO<sub>x</sub> was maximised due to the strong oxygen donation capability of CeO<sub>2</sub> closely connected with Pd species. With the assistance of a hydrophobic Al<sub>2</sub>O<sub>3</sub> support, monodispersed Pd@CeO<sub>2</sub>

structures were obtained. Thus, the agglomeration of the active phase, which caused the generation of hot spots and deactivation of the catalyst by sintering, was avoided.

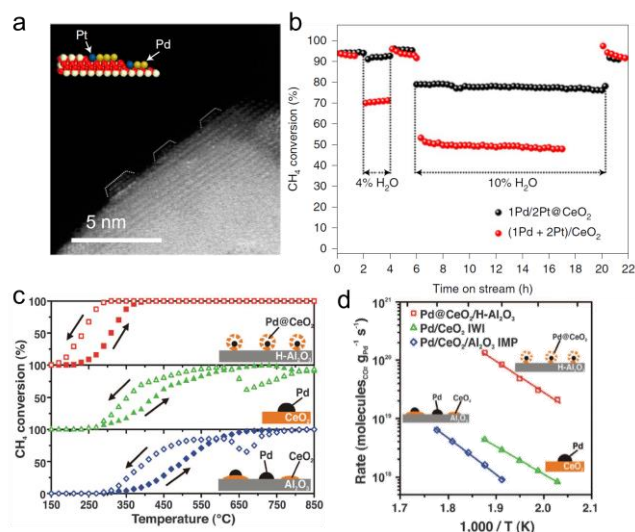


**Figure 4.** (a) TEM image of the 2-D PdO<sub>x</sub> rafts on Pt single atoms anchored CeO<sub>2</sub>, the inset shows the schematic structure of the catalyst; (b) The methane conversion performance of catalysts at 500 °C under different steam concentrations. Reprinted from ref. [76]. Copyright 2021 Springer Nature (colour online). (c) Light-off curves and (d) kinetic rate data of Pd@CeO<sub>2</sub>/H-Al<sub>2</sub>O<sub>3</sub>, Pd/CeO<sub>2</sub> and Pd/CeO<sub>2</sub>/Al<sub>2</sub>O<sub>3</sub>. Reprinted from ref. [77]. Copyright 2012 American Association for the Advancement of Science (colour online).

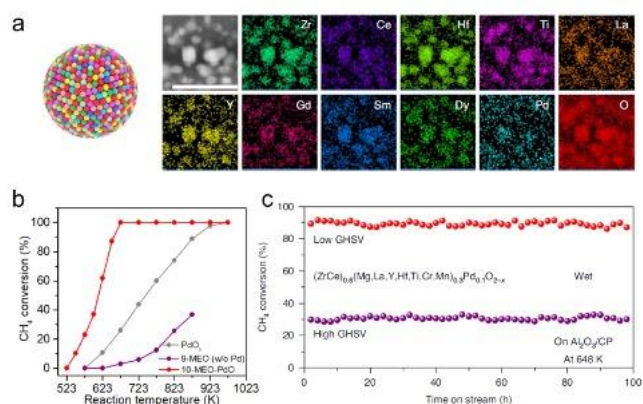


**Figure 5.** (a) A scheme of the single-phase multi-element oxide and the STEM-EDS mapping spectra of a denary (ZrCe)<sub>0.6</sub>(Mg,La,Y,Hf,Ti,Cr,Mn)<sub>0.3</sub>Pd<sub>0.1</sub>O<sub>2-x</sub> oxide; (b) Light-off curves of the denary oxide in comparison with PdO<sub>x</sub> and the oxide without Pd; (c) Long term methane conversion test over the denary oxide in the presence of 4% water vapour at 375 °C under both low and high GHSVs. Reprinted from ref. [78]. Copyright 2021 Springer Nature (colour online).

Very recently, a series of single-phase multi-element oxide nanoparticles were designed and synthesised via a rapid non-equilibrium method [78]. Via rational design and systematic composition tuning of the oxides, a denary (ZrCe)<sub>0.6</sub>(Mg,La,Y,Hf,Ti,Cr,Mn)<sub>0.3</sub>Pd<sub>0.1</sub>O<sub>2-x</sub> oxide was selected and used for catalytic methane oxidation, as shown in

Figure 5a. Complete methane oxidation was reached at 400 °C, which was superior to not only the other quaternary and quinary oxides, but also the PdO<sub>x</sub> reference catalysts (Figure 5b). The nonary oxide without Pd displayed poor catalytic activity, indicating the crucial effect of Pd species in methane oxidation. The denary oxide catalyst also showed excellent thermal and hydrothermal stability. In situ TEM images at 800 °C revealed neither phase separation nor morphology variation. At a high GHSV of 108 000 L g<sub>Pd</sub><sup>-1</sup> h<sup>-1</sup> and in the presence of 4% water vapour, the catalytic methane oxidation performance was maintained for over 100 h (Figure 5c).

Noble metals, such as Pt, Ir, Au, Rh, Ru and Ag were loaded on various support and used for methane oxidation [41–44,79,80]. Pt<sup>0</sup>–Pt<sup>x+</sup> dipoles were observed at the metal-support interface of a Pt/Cr<sub>2</sub>O<sub>3</sub> catalyst [81]. It was claimed that the dipole sites could increase the polarisation of methane molecules and enhance the strength of oriented collisions between the molecules and the catalyst surface. Therefore, the energy barrier required for breaking the first C-H bond in methane was reduced. In addition, the Pt<sup>0</sup>–Pt<sup>x+</sup>

dipole sites are maintained during the catalytic reactions due to the electron donation from the n-type Cr<sub>2</sub>O<sub>3</sub> semiconductor to Pt<sup>0</sup>. The mixed oxidation states of the active phase were also observed in Ag, Ir, and Rh catalysts [42,44,80]. However, no presence of Au<sub>2</sub>O or Au<sub>2</sub>O<sub>3</sub> was detected by the XPS analysis of a Au/Al<sub>2</sub>O<sub>3</sub> catalyst, leaving the metallic Au as the active site for methane oxidation [41].

Currently, noble-metal-based, especially Pd-based materials are still the commercially available and most studied catalysts for methane oxidation due to their high performance. A comparison of the performance of the noble-metal-based thermocatalysts is summarised in Table 1. Considering the scarcity and high cost, the content of noble metals should be reduced to the minimum if they cannot be replaced. The lifetime of commercial catalytic converters in automobiles could be up to 1000 hours under operational conditions or equivalent to 100 000 miles of travelling distance. Thus, the long-term stability (up to 1000 h) of catalysts should be evaluated in future studies.

Table 1 Performance comparison of noble-metal-based thermocatalysts for methane oxidation. T<sub>c</sub> is the temperature at c% methane conversion.

Catalyst	T <sub>c</sub> (°C)	E <sub>a</sub> (kJ/mol)	Feed gas	Stability	Ref.
Pd@Silicalite-1	T <sub>50</sub> =261	114.2	1% CH <sub>4</sub> , 21% O <sub>2</sub> , 78% N <sub>2</sub> , GHSV= 36 000 mL g <sup>-1</sup> h <sup>-1</sup>	-	[53]
Pd-Ce@SiO <sub>2</sub>	T <sub>100</sub> =350	100.4	1% CH <sub>4</sub> , 21% O <sub>2</sub> , 78% N <sub>2</sub> , GHSV= 36 000 mL g <sup>-1</sup> h <sup>-1</sup>	Stable for 25 h H <sub>2</sub> O resistant SO <sub>2</sub> resistant	[57]
Pd/TiO <sub>2</sub>	T <sub>99</sub> =370	83.1	1% CH <sub>4</sub> , 10% O <sub>2</sub> , bal. N <sub>2</sub> , GHSV = 30 000 mL g <sup>-1</sup> h <sup>-1</sup>	Stable for 4 cycles	[59]
Pd/CeO <sub>2</sub>	T <sub>10</sub> =224	-	1% CH <sub>4</sub> , 99% Air, GHSV =50 000 mL g <sup>-1</sup> h <sup>-1</sup>	-	[63]
Pd-Co/BEA	T <sub>50</sub> =352	81.1	1500 ppm CH <sub>4</sub> , 5% O <sub>2</sub> , bal. Ar, GHSV= 99 900 mL g <sup>-1</sup> h <sup>-1</sup>	-	[64]
Pd/SBA-15	T <sub>50</sub> =310	-	0.5% CH <sub>4</sub> , 10.0% O <sub>2</sub> bal. N <sub>2</sub> , GHSV 40 000 mL g <sup>-1</sup> h <sup>-1</sup>	Stable for 5 cycles	[65]
Pd/Na-MOR	T <sub>50</sub> =335	75	1% CH <sub>4</sub> , 4% O <sub>2</sub> , bal. N <sub>2</sub> , GHSV= 70 000 mL g <sup>-1</sup> h <sup>-1</sup>	Stable for 90 h	[66]
Pd/MgAl <sub>2</sub> O <sub>4</sub>	T <sub>50</sub> =337	-	0.5% CH <sub>4</sub> , 10% O <sub>2</sub> , bal. N <sub>2</sub> , GHSV=40 000 mL g <sup>-1</sup> h <sup>-1</sup>	Stable for 90 h	[69]
Pd/Ce <sub>2</sub> Zr <sub>1-x</sub> O <sub>2</sub> -Al <sub>2</sub> O <sub>3</sub>	T <sub>99</sub> =400	92.7	1% CH <sub>4</sub> , 5% O <sub>2</sub> bal. N <sub>2</sub> , GHSV = 50 000 mL g <sup>-1</sup> h <sup>-1</sup>	Stable for 18 h H <sub>2</sub> O resistant	[71]
Au-Pd/ La <sub>0.6</sub> Sr <sub>0.4</sub> MnO <sub>3</sub>	T <sub>50</sub> =331	50.5	5% CH <sub>4</sub> , 30% O <sub>2</sub> , 65 % N <sub>2</sub> , GHSV=50 000 mL g <sup>-1</sup> h <sup>-1</sup>	Stable for 10 h H <sub>2</sub> O resistant	[73]
Pd-Pt/CeO <sub>2</sub>	T <sub>50</sub> =325	74	680 ppm CH <sub>4</sub> , 14% O <sub>2</sub> , 5% CO <sub>2</sub> , bal. N <sub>2</sub> , GHSV=300 000 mL g <sup>-1</sup> h <sup>-1</sup>	Stable for 12 h H <sub>2</sub> O resistant	[76]
Pd@CeO <sub>2</sub> /Al <sub>2</sub> O <sub>3</sub>	T <sub>50</sub> =310	103	0.5% CH <sub>4</sub> , 2.0% O <sub>2</sub> , bal. Ar, GHSV= 200 000 mL g <sup>-1</sup> h <sup>-1</sup>	Stable for 5 cycles	[77]
(ZrCe) <sub>0.6</sub> (Mg,La,Y,Hf,Ti,Cr,Mn) <sub>0.3</sub> Pd <sub>0.1</sub> O <sub>2</sub>	T <sub>100</sub> =400	-	5% CH <sub>4</sub> , 20% O <sub>2</sub> , bal. N <sub>2</sub> , GHSV= 1 080 000 mL g <sup>-1</sup> h <sup>-1</sup>	Stable for 100 h H <sub>2</sub> O resistant	[78]
-x Au/Al <sub>2</sub> O <sub>3</sub>	T <sub>50</sub> =480	73	0.8% CH <sub>4</sub> , 3.2% O <sub>2</sub> , bal. He, GHSV=1 500 h <sup>-1</sup>	-	[41]
Rh/ZrO <sub>2</sub>	T <sub>50</sub> =400	-	1% CH <sub>4</sub> , 2% O <sub>2</sub> , bal. He, GHSV= 15 000 mL g <sup>-1</sup> h <sup>-1</sup>	-	[42]
Ir/TiO <sub>2</sub> -H	T <sub>50</sub> =267	55.5	1% CH <sub>4</sub> , 20% O <sub>2</sub> , bal. N <sub>2</sub> , GHSV=30 000 mL g <sup>-1</sup> h <sup>-1</sup>	Stable for 50 h	[44]
Ag/MnLaO <sub>3</sub>	T <sub>50</sub> =580	74	2% CH <sub>4</sub> , 98% Air, GHSV=120 000 mL g <sup>-1</sup> h <sup>-1</sup>	-	[80]
Pt/Cr <sub>2</sub> O <sub>3</sub>	T <sub>50</sub> =350	-	0.2% CH <sub>4</sub> , 10% O <sub>2</sub> , bal. N <sub>2</sub> , GHSV=30 000 mL g <sup>-1</sup> h <sup>-1</sup>	Stable for 6 cycles	[81]

### 2.1.2 Metal-oxide-based catalysts

Metal oxides, particularly transition metal oxides are important earth-abundant catalysts. Although the performance is usually lower than the Pd-based catalysts, transition metal oxides have been drawing increasing attention due to their cost-effectiveness. Thanks to the multi-chemical-state nature of transition metals, catalytic cycles can easily be

formed between the high and low oxidation states of the metal oxide. Moreover, oxygen release and restore also become possible to facilitate the oxidation reaction. Metal oxides including binary oxides (e.g., Co<sub>3</sub>O<sub>4</sub>, CeO<sub>2</sub>), ternary oxides (e.g., NiCo<sub>2</sub>O<sub>4</sub>, perovskites), multi-element oxides, and their mixtures, have been synthesised and tested for methane oxidation.

Binary oxides, especially those containing multi-valence elements have been intensively studied as methane oxidation catalysts.  $\text{Co}_3\text{O}_4$  nanoparticles with exposed (100), (110) and (111) facets were synthesised by a modified hydrothermal method [82]. The methane oxidation performance of the catalysts followed the order of  $\text{Co}_3\text{O}_4\text{-110} > \text{Co}_3\text{O}_4\text{-100} > \text{Co}_3\text{O}_4\text{-111}$ , with their activation energy being 82.4, 112.8 and 176.2 kJ/mol, respectively. With N-doping into the  $\text{Co}_3\text{O}_4\text{-110}$  by a facial  $\text{N}_2$  plasma engraving method, the performance could be further improved. DFT calculations proved that N doping could activate  $\text{Co}_3\text{O}_4$  by improving the electrophilicity of surface oxygen and lowering the C-H bond activation energy. Smaller nanoparticles with more edge and corner sites usually lead to higher reactivity. Another study also found  $\text{Co}_3\text{O}_4$  with high-index facets could achieve high reaction rates in methane combustion [83]. Highly active  $\text{Co}_3\text{O}_4$  nanocrystals were obtained by in situ oxidation of Co@C core-shell nanocapsules [16]. After the complete burning of carbon shells, enlarged particles of  $\text{Co}_3\text{O}_4$  with a defective surface exposing high-index facets, such as (311) and (220), were obtained. The  $\text{Co}_3\text{O}_4$  interconnecting at the nanoscale created abundant channels for efficient mass transfer of reactants. The 50% methane conversion temperature obtained was as low as 376 °C, which is even comparable to some of the Pd-based catalysts. Other single oxides, such as  $\text{CeO}_2$ ,  $\text{Fe}_2\text{O}_3$  and  $\text{MgO}$  were active in methane oxidation [15,84–86]. Apart from these oxides, hydroxyapatite ( $\text{Ca}_{10}(\text{PO}_4)_6(\text{OH})_2$ ), especially the particles with basal-faceted c-surfaces, was also proved to be active methane oxidation catalysts [87].

Trinary oxides are another group of noble-metal-free methane oxidation catalysts. Perovskites, with a chemical formula of  $\text{ABO}_3$ , are intensively studied in methane oxidation due to their high oxygen mobility, hydrothermal stability and ease of modification. A three-dimensional ordered macroporous  $\text{La}_{0.6}\text{Sr}_{0.4}\text{MnO}_3$  was synthesised using polymethyl methacrylate microspheres as a template [17]. The optimised catalyst displayed a high surface area of 42  $\text{m}^2/\text{g}$ . The 50% methane conversion temperature at GHSV of 30000  $\text{mL g}^{-1} \text{h}^{-1}$  was 560 °C, with an apparent activation energy of 56.6 kJ/mol. Similarly, a mesoporous  $\text{LaCoO}_3$  was prepared by filling a mesopores silica template in a La-Co citrate complex precursor followed by a calcination and silica removal process [88].  $\text{LaCoO}_3$  with a surface area of 96.7  $\text{m}^2/\text{g}$  and an average pore size of 6 nm was obtained.

The high valent cobalt ions and high content of  $\text{O}_2^{2-}/\text{O}^-$  species detected in mesoporous  $\text{LaCoO}_3$  by XPS and TPR analysis resulted in a 50% methane conversion temperature of 470 °C.

Apart from perovskites, oxides like  $\text{NiCo}_2\text{O}_4$ ,  $\text{CoAl}_2\text{O}_4$ ,  $\text{MgFe}_2\text{O}_4$ , etc., with a spinel lattice structure were also important methane oxidation catalysts [89–91]. Among them,  $\text{NiCo}_2\text{O}_4$  was the most active and well-studied.  $\text{NiCo}_2\text{O}_4$  nanoparticles could achieve 100% methane oxidation at the temperature of 350 °C, while the reference  $\text{Co}_3\text{O}_4$  and  $\text{NiO}$  catalysts only displayed less than 10% of methane conversion [92]. More importantly, the performance of  $\text{NiCo}_2\text{O}_4$  catalysts was also excellent when replacing the dry methane with the exhaust from the engine of natural gas vehicles. Recently,  $\text{NiCo}_2\text{O}_4$  with various morphologies, such as nanoplates, nanocubes, pyramidal nanosheets and bowtie-shaped nanocrystals, were synthesised by using different capping agents [93]. The bowtie-shaped  $\text{NiCo}_2\text{O}_4$  catalyst displayed the highest performance and achieved 100% methane conversion at 410 °C with a GHSV of 90000  $\text{mL g}^{-1} \text{h}^{-1}$ . However, the water resistance of the catalyst needs to be further improved as the conversion of methane decreased from 76% to ~30% when 5% of water was introduced into the reaction atmosphere.

Fruitful achievement has been obtained for the development of noble-metal-free catalysts for methane oxidation over the past decades. However, the performance of transition-metal-oxide-based catalysts is considerably lower than the Pd-based materials. A summary of the performance of transition-metal-oxide-based thermocatalysts is listed in Table 2. Although light-off points lower than 300 °C were reported over certain catalysts, the reaction condition applied was far from the industrial requirement (e.g., low methane concentration and gas hourly space velocity). Thus, the major challenge is still the development of high-performance transition-metal-oxide-based catalysts that effectively work at low temperatures. Moreover, it is appealed that similar reaction conditions as assessing the Pd-based materials should be applied to evaluate the performance of noble-metal-free catalysts. Thus, readers could have a comprehensive understanding of the true performance of a newly developed catalyst.

Table 2 Performance comparison of transition-metal-oxide-based thermocatalysts for methane oxidation. Tc is the temperature at c% methane conversion.

Catalyst	Tc (°C)	Ea (kJ/mol)	Feed gas	Stability	Ref.
$\text{Co}_3\text{O}_4$	$T_{50}=376$	68	6.7% $\text{CH}_4$ , 16.8% $\text{O}_2$ , bal. He, GHSV=18 000 $\text{mL g}^{-1} \text{h}^{-1}$	Stable for 25 h	[16]
N- $\text{Co}_3\text{O}_4$	$T_{50}=342$	73.0	2% $\text{CH}_4$ , 20% $\text{O}_2$ , 5% $\text{H}_2\text{O}$ , bal. Ar, GHSV = 46 800 $\text{mL g}^{-1} \text{h}^{-1}$	Stable for 10 h $\text{H}_2\text{O}$ resistant	[82]
$\text{Co}_3\text{O}_4$	$T_{50}=313$	-	2% $\text{CH}_4$ , 98% air, GHSV=24 000 $\text{mL g}^{-1} \text{h}^{-1}$	-	[83]
$\alpha\text{-Fe}_2\text{O}_3$	$T_{50}=366$	-	5% $\text{CH}_4$ , 20% $\text{O}_2$ , bal. Ar, GHSV=10 000 $\text{mL g}^{-1} \text{h}^{-1}$	Stable for 10 h	[84]
$\text{MgO}$	$T_{50}=225$	-	1% $\text{CH}_4$ , 99% Air, 1 mL cat., GHSV=6 000 $\text{mL h}^{-1}$	Stable for 70 h	[85]

LaCoO <sub>3</sub>	T <sub>50</sub> =470	-	0.8% CH <sub>4</sub> , 5% O <sub>2</sub> , bal. N <sub>2</sub> , GHSV=60 000 mL g <sup>-1</sup> h <sup>-1</sup>	-	[88]
NiCo <sub>2</sub> O <sub>4</sub>	T <sub>50</sub> =280	59	1% CH <sub>4</sub> , 99% Air, GHSV=24 000 mL g <sup>-1</sup> h <sup>-1</sup>	Stable for 12 h	[90]
NiCo <sub>2</sub> O <sub>4</sub>	T <sub>100</sub> =350	-	5% CH <sub>4</sub> , 25% O <sub>2</sub> , bal. Ar, GHSV=24 000 mL g <sup>-1</sup> h <sup>-1</sup>	Stable for 48 h H <sub>2</sub> O resistant	[92]
NiCo <sub>2</sub> O <sub>4</sub>	T <sub>100</sub> =410	-	1000 ppm CH <sub>4</sub> , 10% O <sub>2</sub> , bal. Ar, GHSV=90 000 mL g <sup>-1</sup> h <sup>-1</sup>	Stable for 12 h H <sub>2</sub> O resistant	[93]
La <sub>0.6</sub> Sr <sub>0.4</sub> MnO <sub>3</sub>	T <sub>50</sub> =566	56.6	2% CH <sub>4</sub> , 20% O <sub>2</sub> , bal. N <sub>2</sub> , GHSV=30 000 mL g <sup>-1</sup> h <sup>-1</sup>	-	[17]
CoAlO <sub>x</sub> /CeO <sub>2</sub>	T <sub>50</sub> =415	92.2	10% CH <sub>4</sub> , 25% O <sub>2</sub> , bal. Ar, GHSV=24 000 mL g <sup>-1</sup> h <sup>-1</sup>	Relatively stable for 50 h	[91]

### 2.1.3 Catalyst deactivation

The lifetime of catalysts is directly related to the economics of an industrial catalytic process. Therefore, the durability is an important aspect to evaluate the overall performance of a thermocatalyst for methane combustion. The factors that cause catalyst deactivation could include one or a few issues listed here. The high operating temperature increases the atomic mobility of both the noble metals and the support, causing decomposition or sintering of the active phase. A high concentration of water under the real application conditions preferentially adsorbs on the active sites and forms either hydroxide groups or inactive phases with the noble metals. Some other components, such as sulfur compounds or carbon dioxide could poison the active sites and cause catalyst deactivation.

High temperature caused sintering and/or coking is an important origin for catalyst deactivation. It should be noted that sintering occurs on both the catalyst and the support. Sintering of the catalyst causes the reduction of active sites and formation of inactive phases. While sintering of the support reduces the surface area and dispersion of the catalyst. For Pd-based catalysts, it is acknowledged that PdO is the active phase, which is converted to metallic Pd at high temperatures. Several methods have been developed to improve the thermal stability of catalysts. The most direct and effective way is to develop catalysts that work at lower temperatures (e.g., < 300 °C). Apart from this, using reducible oxides (e.g., CeO<sub>2</sub>) and/or transition metal oxides (e.g., Co<sub>3</sub>O<sub>4</sub>) as a support could mitigate the reduction of the active PdO phase [63,94]. Applying another metal in the catalyst or using mixed support can also significantly improve the thermostability of methane oxidation catalysts. For instance, a denary oxide (ZrCe)<sub>0.6</sub>(Mg,La,Y,Hf,Ti,Cr,Mn)<sub>0.3</sub>Pd<sub>0.1</sub>O<sub>2-x</sub> displayed excellent thermostability at a high temperature of 800 °C [78]. The methane oxidation performance of the catalyst was maintained for 100 h without noticeable deterioration. Apart from the chemical modifications, the physical confinement of the active catalyst could also improve the sintering resistance of catalysts. Pd@CeO<sub>2</sub> core-shell nanostructures supported on Al<sub>2</sub>O<sub>3</sub> displayed superior performance and stability compared with the physical mixture of Pd/CeO<sub>2</sub> on Al<sub>2</sub>O<sub>3</sub> [77]. Pd nanoparticles embedded in the zeolite displayed superior stability compared with the catalyst sup-

ported on the same support [53]. Similarly, Pd-exchanged zeolite was also reported to not only reduce the reaction temperature but also improve the thermostability of the catalysts [95].

Under the actual application conditions, the reaction atmosphere for catalytic methane oxidation contains a large amount of water (10% to 15%). Water vapour at high temperatures acts as a promoter for catalyst sintering. Moreover, due to its polarity, water molecules, instead of methane, are preferentially adsorbed on the active sites, hindering the activation of methane. Water vapour in methane oxidation atmosphere also causes side reactions such as the steam reforming of methane and water gas shift reaction, which reduce the efficiency of the catalytic process. It was reported that water formed hydroxide radicals and/or reacted with the active PdO to form inactive Pd(OH)<sub>2</sub> under reaction conditions [96]. The inhibition of methane oxidation by water vapour was reported to be less effective under higher temperatures (e.g., > 500 °C) since desorption of hydroxyl groups became a facile process [97]. In a methane oxidation system based on Pd/SBA-15 catalyst, the methane conversion rate only dropped from 96% to 84% at 450 °C. In contrast, at 350 °C, the conversion of methane reduced to as low as 8% from 52% [65]. Since catalysts with a low operating temperature are ideal in thermocatalytic methane oxidation, it is not sensible to apply high temperatures to reduce the disadvantage of water vapour. As hydrothermally induced sintering is the main cause of catalyst deactivation from water vapour, the stabilisation of catalysts on the support could be an effective strategy to reduce the adverse effect of water. Pd aggregates in the confined space of H-ZSM-5 displayed improved water resistance capability compared with Pd nanoparticles on H-ZSM-5 zeolite [98]. Very recently, a Pd-Pt on CeO<sub>2</sub> catalyst was reported to exhibit superior stability against water vapour [76]. As shown in Figure 6, both performances of 1Pd/CeO<sub>2</sub> and 2Pt@CeO<sub>2</sub> displayed poor stability in the presence of 4% H<sub>2</sub>O. On the contrary, with the co-existence of Pd and Pt, the stability of (1Pd+2Pt)/CeO<sub>2</sub> only showed a slight reduction from 79% methane conversion to 73% after 12 h. Furthermore, when a special geometry of Pd-Pt structure was formed, the high methane conversion of 95% could be maintained for at least 12 h without noticeable deactivation. The excellent methane oxidation performance and water tolerance capability of (1Pd+2Pt)/CeO<sub>2</sub> were ascribed to low methane activation

energy and high water dissociation energy of the Pd-Pt structure on CeO<sub>2</sub>.

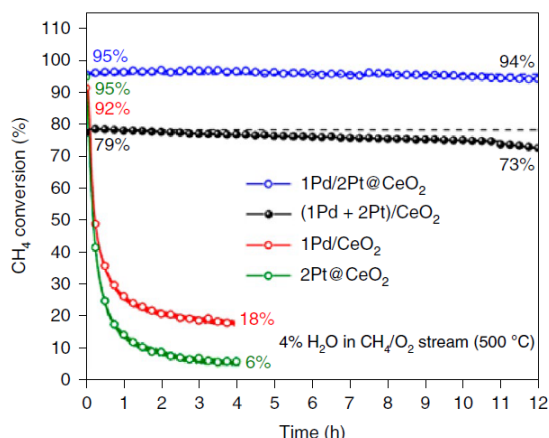


Figure 6 Comparison of catalyst stability for the as-synthesised 1Pd/2Pt@CeO<sub>2</sub> and (1Pd+2Pt)/CeO<sub>2</sub> catalysts, 2Pt@CeO<sub>2</sub> and 1Pd/CeO<sub>2</sub> catalysts in CH<sub>4</sub> oxidation at 500 °C with 4% H<sub>2</sub>O. Reprinted from ref. [76]. Copyright 2021 Springer Nature (colour online).

Natural gas contains certain levels of sulphur compounds, which may exist as H<sub>2</sub>S, SO<sub>2</sub>, SO<sub>3</sub> and SO<sub>4</sub><sup>2-</sup> during methane oxidation depending on the reaction conditions. Sulphur compounds, especially SO<sub>2</sub>, can poison most noble metals (e.g., Pd, Rh, etc.) even at the concentration of ppm level. However, Pt is an excellent catalyst for SO<sub>2</sub> oxidation, thus it can be used to improve the sulfur tolerance capability of Pd-based methane oxidation catalysts [33,99]. Poisoning of catalysts by SO<sub>2</sub> occurs via either competitive adsorption at the active sites, or by sulfation of the active phase and/or support. It was reported that SO<sub>2</sub> competed with CH<sub>4</sub> for adsorption sites on PdO-Al<sub>2</sub>O<sub>3</sub> surfaces [100]. The formation of PdSO<sub>4</sub> and Al<sub>2</sub>(SO<sub>4</sub>)<sub>3</sub> was also observed using FTIR when SO<sub>2</sub> was introduced in the methane oxidation reaction [101]. To regenerate the active phase, thermal treatment of catalysts under vacuum or in a reductive atmosphere (e.g., H<sub>2</sub> and CH<sub>4</sub>) can remove the sulphate groups by releasing SO<sub>2</sub> [33,102]. It has been reported that some catalysts (e.g., Pd@ZrO<sub>2</sub>) displayed relatively high sulfur poisoning resistance [103]. However, catalyst deactivation by sulfur poisoning is a complicated process and research on the deactivation mechanism and development of sulfur-resistant catalysts are still challenging.

CO<sub>2</sub> could also introduce inhibitory effects on the performance of methane oxidation, and normally a high concentration of CO<sub>2</sub> exists in the real application. However, in the co-existence of CO<sub>2</sub> and H<sub>2</sub>O, only the adverse effect of H<sub>2</sub>O was observed [35]. The reduction in methane performance caused by CO<sub>2</sub> alone is also less significant than other additives. Thus, the effect of CO<sub>2</sub> was not investigated as much as other compounds.

Catalyst deactivation is a complex yet important process in catalytic methane oxidation. Fundamental studies on cat-

alyst deactivation guide future catalyst design and prolong the catalyst lifetime, thus reducing the capital costs of the catalytic process. The current research results are far from the full understanding of catalyst deactivation. Thus, it is encouraged that evaluation of catalyst performance should be carried out under real application conditions. The studies on the effect of poisonous additives on the performance should also be considered in future studies.

## 2.2 Fundamental understandings

Fundamental studies via in situ and/or operando technologies reveal the details of the catalytic process and provide significant information for catalyst design and practical application. Current fundamental understandings in thermo-catalytic methane conversion include the catalyst structure evolution, which describes the active sites/phase and the structural information of catalysts during the reaction, and intermediate detection, which guides the reaction pathway study and control of product yield and selectivity.

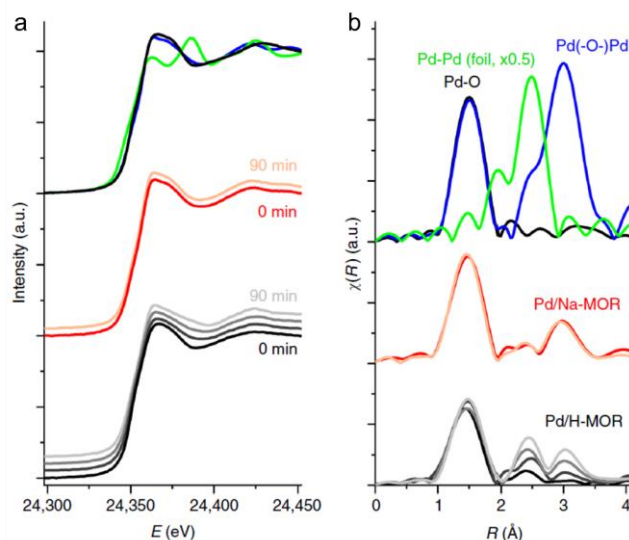
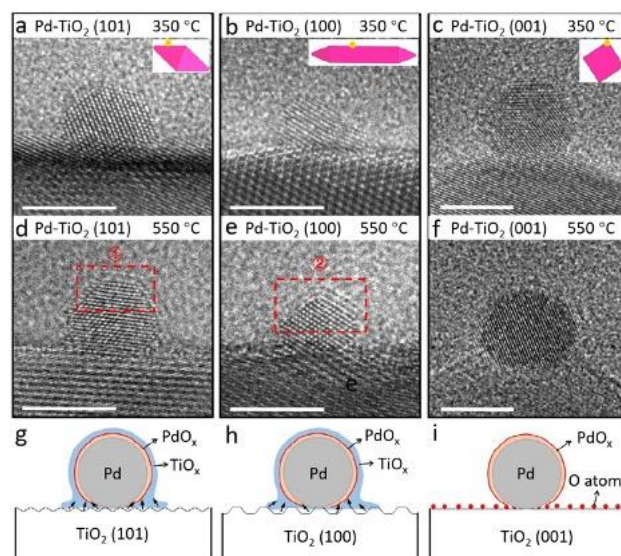


Figure 7. (a) XANES spectra and (b) the corresponding Fourier transforms of in situ Pd K-edge EXAFS spectra of the catalysts after pretreatment (10 min in 1 vol% CH<sub>4</sub>, 4 vol% O<sub>2</sub>, balance N<sub>2</sub>, GHSV= 350 000 h<sup>-1</sup> at 410 °C) and after 15, 30, and 90 min ageing in a feed of 1 vol% CH<sub>4</sub>, 4 vol% O<sub>2</sub>, 5 vol% H<sub>2</sub>O, balance N<sub>2</sub> at 410 °C: Pd/H-MOR (black to light grey); Pd/Na-MOR (red to pink). Reprinted from ref. [66]. Copyright 2018 Springer Nature (colour online).

To study the structure information of the catalysts, in situ and/or operando technologies such as X-ray absorption spectroscopy (XAS), X-ray photoelectron spectroscopy (XPS), transmittance electron microscopy (TEM), X-ray diffraction (XRD) and Raman spectroscopy have been applied to investigate the structural evolution of catalysts in the catalytic reaction conditions. In situ XPS spectra of O 1s and Pd 3d in a heating and cooling process from 127 °C to 527 °C in the presence of CH<sub>4</sub> and O<sub>2</sub> (CH<sub>4</sub> : O<sub>2</sub> = 1:5) were performed to study the chemical states of Pd and O in Pd catalyst [104]. It was found that PdO seeds in the catalysts

formed at 227-377 °C were the active sites for methane oxidation. A performance-structure relationship was well-established. In situ XAS was applied to study the hydrothermal resistance performance of Pd-MOR catalyst, as shown in Figure 7. The X-ray absorption near edge structure (XANES) spectra of the catalyst were obtained in a CH<sub>4</sub>, O<sub>2</sub>, N<sub>2</sub> and H<sub>2</sub>O mixture flow at 410 °C for a certain time [66]. Due to the strong metal support interaction between the Pd metal and Na-exchanged MOR zeolite, the Pd-O structure was more stable than that of the reference Pd-loaded MOR zeolite. The formation of Pd-Pd bond was detected, which was the result of PdO<sub>x</sub> reduction in Pd/H-MOR. In contrast, Pd/Na-MOR showed robust structure stability of PdO<sub>x</sub> (Figure 7b). The results indicated that the deactivation of catalysts in the presence of water was due to the reduction of the active PdO<sub>x</sub> to metallic Pd. In situ XRD and Raman spectroscopy were also applied to investigate the chemical states of Pd, which provide important information in determining the active phase of Pd in methane oxidation [40,105,106].

Apart from advanced spectroscopies, TEM was also used to gain a direct observation of the structure and composition information of the catalyst in simulated reaction conditions. In situ TEM was applied to study the structure stability of a denary metal oxide catalyst [78]. The oxide was heated from 25 to 800 °C while the catalyst maintained uniform mixing without phase separation and showed superior structural stability. Recently, in situ TEM was used to directly observe the metal-support interaction between Pd and TiO<sub>2</sub> under oxidative conditions [50]. It is generally thought that TiO<sub>2</sub> is reduced at high temperatures, and then the formed unstable TiO<sub>x</sub> species migrate onto the metal surface forming metal NPs encapsulated by the TiO<sub>x</sub> layers [107]. TiO<sub>2</sub> with exposed (101), (100) and (001) facets were used as supports. The Pd-loaded TiO<sub>2</sub> catalysts were observed in an ambient pressure TEM, as shown in Figure 8. The Pd surface was clear in all three catalysts at the temperature of 350 °C (Figure 8 a-c). When the temperature was increased to 550 °C, obvious encapsulations were formed on the Pd NPs supported on TiO<sub>2</sub> (101) and TiO<sub>2</sub> (100) surfaces (Figure 8 d-e). However, no evident structural change was observed for TiO<sub>2</sub> (001) supported Pd (Figure 8f). This indicated that the encapsulations were facet dependent. To identify the nature of the encapsulations, aberration corrected environmental STEM were used. The interplanar spacing measurement, combined with the electron energy-loss spectroscopy suggested that the surface layer was PdO<sub>x</sub> and TiO<sub>x</sub> for Pd-TiO<sub>2</sub> (101) and Pd-TiO<sub>2</sub> (100), while only PdO<sub>x</sub> for Pd-TiO<sub>2</sub> (001). The reason for the formation of such metal support interaction was explained by the surface energy of the support. The TiO<sub>2</sub> (001) with a high surface energy was prone to be covered by O<sub>2</sub> under oxidative conditions, which hindered the migration of surface Ti atoms, therefore displaying a low metal support interaction (Figure 8 g-i).



**Figure 8.** (a-f) In situ TEM images of Pd-TiO<sub>2</sub> catalysts with exposed facets under oxidative conditions (O<sub>2</sub> 20 vol%/ N<sub>2</sub> at 1 atm) at different temperatures, scale bar 5 nm; (g-i) Proposed model for facet-dependent oxidative metal-support interaction. Reprinted from ref. [50]. Copyright 2021 John Wiley and Sons Ltd. (colour online).

Understanding the reaction pathway helps to tune the product selectivity, therefore guiding the catalyst design. Methyl radical is generally understood as the product of methane activation, and the intermediate for later radical reactions in all methane conversion processes. In situ electron spin resonance (ESR) spectroscopy can be used to detect methyl radicals in the selective oxidation of methane to produce hydrocarbons [108]. Diffuse reflectance infrared Fourier transform spectroscopy (DRIFTS) has been widely used to observe the intermediates formed in catalytic methane oxidation, as the organic species on the surface of the catalysts are very sensitive to IR. In most studies, methane oxidation follows a formate pathway [92,109]. In this process, O<sub>2</sub> is firstly adsorbed and activated on the catalyst surface, forming reactive oxygen species, which are then used to activate methane and result in the formation of methoxyl radicals and OH radicals. The subsequent dehydration causes the formation of formate radicals, which are finally oxidised to carbon dioxide. Since water has a strong IR absorption, in situ DRIFTS at high temperatures could also be used to study the water resistance property of methane oxidation catalysts [61], as water-resistant catalysts display low water adsorption capability.

XPS is a powerful technology for surface analysis, which has been used to study the surface species formed in methane oxidation. The ratio of C to (Ni+Co) on the surface of NiCo<sub>2</sub>O<sub>4</sub> catalyst was measurement from the ambient pressure XPS carried out in the presence of CH<sub>4</sub> and O<sub>2</sub> at various temperatures [92]. It was observed that the number of

carbon species with a binding energy of 288.3 eV decreased at the temperature from 200 to 300 °C, during which period a rapid increase in methane conversion was observed. Therefore, this species was identified as the intermediate in methane oxidation. However, the nature of this intermediate was not discussed. Very recently, the same technology was applied in methane oxidation using IrO<sub>2</sub> film as the catalyst [110]. In the O 1s spectrum (Figure 9a), it was found that surface OH groups were bound directly to the initially, coordinatively unsaturated Ir atoms. The formation of such excess OH groups suggested that dissociative adsorption of O<sub>2</sub> was more facile than CH<sub>4</sub> activation and conversion. In the C 1s spectrum under 90% CH<sub>4</sub> and 10% O<sub>2</sub> atmosphere, a surface species with a CH<sub>y</sub>O<sub>z</sub> stoichiometry was observed as an intermediate in the methane oxidation process (Figure 9b). This provided direct evidence for the identification of intermediate species in methane oxidation and was in accordance with the DRIFTS analysis in many previous reports [92,109].

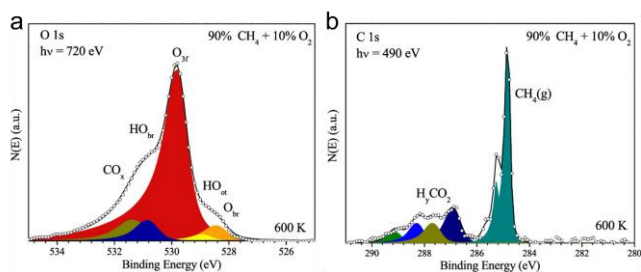


**Figure 9.** Ambient pressure XPS (a) O 1s and (b) C 1s spectra obtained from IrO<sub>2</sub> (110) film under CH<sub>4</sub> and O<sub>2</sub> atmosphere at 327 °C. Reprinted from ref. [110]. Copyright 2022 American Chemical Society (colour online).

### 3 Photocatalytic methane oxidation

Although enormous progress has been achieved in methane oxidation by thermocatalysis, the high temperature required makes the process energy intensive and causes the formation of toxic NO<sub>x</sub> under such conditions. With the energy from photons, many reactions that require harsh conditions can be operated under mild conditions. For instance, photon-assisted thermal catalytic methane oxidation over CeO<sub>2</sub>- and MCM-41-based catalysts was developed [111,112]. The 50% methane conversion temperature has been reduced to as low as 240 and 170 °C, respectively. More importantly, the oxidation of methane has been realised via direct photocatalysis under ambient conditions (room temperature and atmospheric pressure). Although photocatalytic methane oxidation has not been studied intensively as the thermocatalytic process, current important progress achieved has displayed its potential in the oxidation of methane. Semiconductor-based materials, usually decorated with co-catalysts, are used for photocatalytic methane oxidation. The semiconductor acts as a light-absorbent, which absorbs photons

and generates electron-hole pairs for reactant activation and subsequent conversion reactions. The co-catalysts, which could be noble metals and transition metal oxides, are loaded onto the semiconductor surface to improve charge separation and/or reactant activation. The development of methane oxidation photocatalysts will be discussed according to the different catalysts used. The fundamental studies to understand the charge transportation and reaction pathway in photocatalytic methane oxidation process will also be summarised.

#### 3.1 Photocatalyst development

The first report of methane oxidation by photocatalysis can be dated back to 1978 [25]. TiO<sub>2</sub> was irradiated under a Hg lamp in pure methane at room temperature. The main products obtained were CO and CO<sub>2</sub>, with a small amount of C<sub>2</sub>H<sub>6</sub>. The overall methane conversion rate and product yield were very low. After that, TiO<sub>2</sub> has been modified in various procedures, such as co-catalysts loading, morphology control, facet engineering and formation of heterostructures to improve its activity for methane oxidation. For co-catalyst loading, Pt, Pd, Ru, Zn and SrCO<sub>3</sub> were reported to be effective co-catalysts on TiO<sub>2</sub> that can selectively convert methane into CO<sub>2</sub>, mainly owing to the strong oxygen reduction capability of the co-catalysts [26,113–116]. Vertically aligned TiO<sub>2</sub> nanotube arrays were grown on Pyrex lids via anodic oxidation [117]. It was found that as the thickness of the film increased, the methane oxidation performance first increased and peaked at 575 nm thickness, and then decreased when the film was further thickened. Very recently, TiO<sub>2</sub> nanosheets, nanorods and octahedrons with exposed {001}, {100} and {101} facets were synthesised and tested for methane oxidation by us (Figure 10 a-c) [118]. A high methane oxidation rate of 17.6 mmol h<sup>-1</sup> g<sup>-1</sup> was obtained over TiO<sub>2</sub>-{001}, which is 6 and 7 times that of the TiO<sub>2</sub>-{100} and TiO<sub>2</sub>-{101}, as shown in Figure 10d. The performance achieved was even higher than that of a Pt loaded anatase TiO<sub>2</sub> catalyst (Figure 10e). The improved performance was resulted from the unique and fast bulk-surface charge transportation and facile methane oxidation of the TiO<sub>2</sub>-{001} photocatalyst. The details will be discussed later in the fundamental understanding part. Another strategy to improve the photocatalytic methane oxidation performance of TiO<sub>2</sub> is by formation of heterostructures, which could promote charge separation and migration. Recently, a series of biphasic heterostructured photocatalysts containing anatase and rutile TiO<sub>2</sub> were reported for methane oxidation [119]. In the absence of water, CO<sub>2</sub> was produced solely at a rate of 6.8 mmol/g<sub>cat.</sub> in 3 h in 20 bar CH<sub>4</sub> and 5 bar O<sub>2</sub> over the optimised catalyst (90% anatase and 10% rutile TiO<sub>2</sub>). The formation of the heterostructure promoted charge separation and migration between the two phases of TiO<sub>2</sub>, thus improving the performance of methane oxidation. Up to now, MoO<sub>3</sub>, SiO<sub>2</sub> and ZnO were reported

to have positive effects on the methane oxidation performance when forming a heterojunction with  $\text{TiO}_2$  [114,120,121].

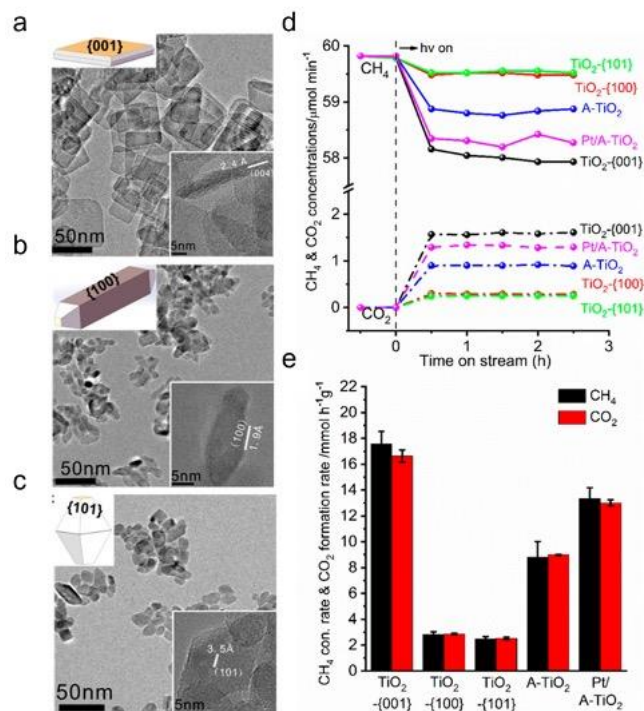


**Figure 10.** (a-c) TEM images of  $\text{TiO}_2$  nanocrystals with exposed {001}, {100} and {101} facets; (d)  $\text{CH}_4$  conversion and  $\text{CO}_2$  production with time and (e) methane oxidation performance of  $\text{TiO}_2$  nanocrystals, commercial anatase, and Pt loaded anatase. Reprinted from ref. [118]. Copyright 2022 American Chemical Society (colour online).

$\text{ZnO}$ , a semiconductor with a similar band structure as  $\text{TiO}_2$ , has drawn increasing attention in recent years. Due to its intrinsic in-built electric field resulting from the non-uniform charge distribution,  $\text{ZnO}$  displays a large spontaneous polarisation of  $0.047 \text{ C m}^{-2}$  along the [0001] direction [122]. This structure is not only beneficial for charge separation but also favourable for the facile activation of methane (Figure 11a) [123–125]. Defective-rich  $\text{ZnO}$  nanoparticles loaded with Ag were used for methane oxidation [123]. The defects in  $\text{ZnO}$  could improve the surface reaction during photocatalysis, and silver acted both as a light absorbent and charge separator (Figure 11b). The defective  $\text{ZnO}$  was active in methane oxidation under both UV and visible light, while commercial  $\text{ZnO}$  and P25  $\text{TiO}_2$  could only oxidise methane in the presence of UV light (Figure 11c). The performance of Ag decorated  $\text{ZnO}$  in UV-Vis irradiation was higher than that under UV or visible light, suggesting a synergy between  $\text{ZnO}$  and the plasmonic Ag. A similar effect was also observed in Au- $\text{ZnO}$  photocatalyst for non-oxidative coupling of methane [122]. Ag- $\text{ZnO}$  completed the oxidation of 100 ppm methane in 25 min, achieving a quantum yield of 8% at  $\lambda < 400 \text{ nm}$ . The

methane oxidation reaction was also tested in a flow reactor. The methane concentration dropped close to zero while carbon dioxide was formed immediately after light irradiation (Figure 11d). Combined with the fact that CO and hydrocarbons were not detected, a good carbon balance was achieved in the reaction. It has been proved that Ag, Au, Pd and Cu were all efficient co-catalysts on  $\text{ZnO}$  for methane oxidation [27,28,126–128].

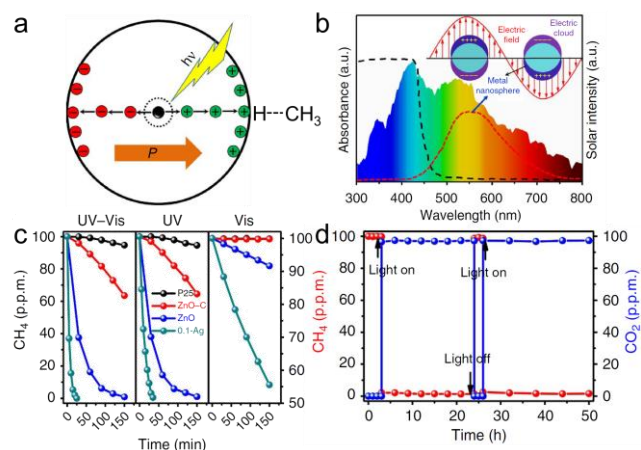


**Figure 11.** (a) A scheme showing the intrinsic electric field generated in  $\text{ZnO}$  and its effect on charge separation and methane activation; (b) Effect of Ag nanoparticle as a light absorbent and a co-catalyst; (c) Photocatalytic methane oxidation performance of  $\text{ZnO}$ -based catalysts and commercial P25  $\text{TiO}_2$  under different light source; (d) Photocatalytic methane oxidation performance under UV-Vis light in a flow reactor at a total flow rate of 25 mL/min. Reprinted from ref. [123]. Copyright 2016 Springer Nature (colour online).

Apart from the widely used  $\text{TiO}_2$  and  $\text{ZnO}$ ,  $\text{SrTiO}_3$ ,  $\text{BiVO}_4$ ,  $\text{AgCl}$  and some other catalysts were also applied in photocatalytic methane oxidation [29,30,129–131].  $\text{SrTiO}_3$  catalysts were synthesised by sol-gel method ( $\text{SrTiO}_3$ -S), calcination method ( $\text{SrTiO}_3$ -C) and hydrothermal method ( $\text{SrTiO}_3$ -H) [30]. Only  $\text{SrTiO}_3$ -S was capable of photocatalytic methane oxidation, while  $\text{SrTiO}_3$ -C and  $\text{SrTiO}_3$ -H were inactive. It was found that  $\text{SrCO}_3$ , which acted as a co-catalyst in methane oxidation, was formed on the surface of  $\text{SrTiO}_3$  during the sol-gel preparation process. After the decoration of  $\text{SrCO}_3$ , the adsorption of methane and desorption of oxidation product ( $\text{CO}_2$ ) were improved in  $\text{SrTiO}_3$ -S compared with other  $\text{SrTiO}_3$  catalysts. However, the temperature programmed desorption experiment could be modified to provide more solid evidence for this conclusion.  $\text{CO}_2$  was detected in the products of methane oxidation by  $\text{BiVO}_4$  [131]. The overall performance of quantum-sized  $\text{BiVO}_4$  was much higher than that of  $\text{BiVO}_4$  sub-micron particles. With the partial pressure of  $\text{O}_2$  gas increased, the production of  $\text{CO}_2$  also improved. The oxidation process followed a  $\text{CH}_4 \rightarrow \text{CH}_3\text{OOH} \rightarrow \text{CH}_3\text{OH} \rightarrow \text{HCHO} \rightarrow \text{CO}_2$  with  $\text{OH}\cdot$  radicals as the main oxidants in each step. Ag/AgCl was synthesised by the photo-decomposition of AgCl and tested for methane oxidation in a quartz reactor [29]. Low activities were observed with either UV or visible

light, while the performance under UV-visible light was significantly improved. This indicated a synergistic effect between AgCl and the plasmonic Ag. Recently, a methane gas sensor based on  $Ti_2CT_x$  MXene was fabricated [129]. The assembled detector displayed much higher response and selectivity under visible light irradiation than in dark. The gas sensing mechanism was due to methane oxidation to carbon dioxide, as proved by photocatalytic oxidation reactions and in situ DRIFTS characterisation.

Photocatalysis has opened a new and green pathway for the treatment of the environmental issues caused by methane emission. The performance of the currently reported methane oxidation photocatalysts is summarised in Table 3. Future studies on photocatalytic methane oxidation should still be focused on the development of high-efficiency catalysts as the performance of photocatalytic methane oxidation processes is much lower than the traditional thermoca-

talysis. Moreover, the catalysts used are mainly  $TiO_2$ - and ZnO-based semiconductors, which are only responsive to UV light. The discovery of visible responsive catalysts (e.g., organic catalysts, Z-scheme heterostructures) could broaden the absorption of light energy to achieve high efficiency. Another important issue that should be addressed is that the reaction conditions of photocatalytic methane oxidation reaction, such as the light source, methane concentration, etc., should be unified to reveal the intrinsic activity of different catalysts. Finally, the stability test in photocatalytic methane oxidation is inadequate or even overlooked in some studies. The durability and anti-photo-corrosion performance of catalysts should be measured as the future application of the photocatalytic process would require robust and stable catalytic systems.

Table 3 Performance comparison of photocatalysts for methane oxidation.  $Sc_{CO_2}$  is the selectivity of  $CO_2$  in the products.

Catalyst	Reaction conditions	Yield ( $\mu\text{mol/h}$ )	$Sc_{CO_2}$ (%)	Ref.
$TiO_2$	Batch reactor, 1300 ppm $CH_4$ in air, Hg lamp, RT	3.9	11	[25]
$TiO_2$	Batch reactor, 3 bar $CH_4$ , Xe lamp, RT	1.1	100	[115]
$TiO_2$	Batch reactor, 20 bar $CH_4$ , 5 Bar $O_2$ , Xe lamp, RT	23	100	[119]
Pt/ $TiO_2$	Flow reactor, 1 bar, 365 nm LED, RT	9	80	[132]
$SrCO_3/TiO_2$	Batch reactor, 1 bar, Xe lamp, RT	0.2	-	[26]
Pd-HPW/ $TiO_2$	Batch reactor, 3 bar $CH_4$ , 1 bar air, Xe lamp, RT	38	100	[113]
Pt-ZnO/ $TiO_2$	Flow reactor, 1 bar, $CH_4=69$ mL/min, air=1 mL/min, Xe lamp, 140 °C	144	100	[114]
ZnO	Batch reactor, 1 bar, 250 ppm $CH_4$ in air, Xe lamp, RT	2	100	[124]
Ag/ZnO	Batch reactor, 1 bar, 250 ppm $CH_4$ in air, Xe lamp, RT	22	100	[27]
Ag/ZnO	Batch reactor, 1 bar, 100 ppm $CH_4$ in air, Xe lamp, RT	4.8	100	[123]
CuO/ZnO	Batch reactor, 1 bar, 100 ppm $CH_4$ in air, Xe lamp, RT	4	100	[28]
Pd-rGO/ZnO	Batch reactor, 1 bar 20 ppm $CH_4$ in air, 470 nm irradiation, RT	0.1	-	[126]
Au-CeO <sub>2</sub> /ZnO	Batch reactor, 1 bar, 250 ppm $CH_4$ in air, Xe lamp, RT	0.6	100	[128]
Ag/AgCl	Batch reactor, 1 bar, 500 ppm $CH_4$ in air, Xe lamp, RT	5.4	100	[29]
$SrCO_3/SrTiO_3$	Batch reactor, 1 bar, 200 ppm $CH_4$ in air, Xe lamp, RT	0.8	100	[30]
$BiVO_4$	Batch reactor, 1 bar, 20 ppm $CH_4$ in air, visible light, RT	0.05	-	[129]

### 3.2 Fundamental understanding

Fundamental studies in photocatalytic methane oxidation are essential to reveal the photophysics and surface chemistry involved to guide future research in catalyst design and process engineering. Since methane oxidation by photocatalysis is a newly developed technology, the research in this field is focused on new catalyst development. Only very few reports mentioned the fundamental mechanisms, such as the charge separation, reaction intermediates and reaction pathway.

We firstly used the in-situ UV-Vis-NIR technique to study the behaviour of photogenerated electrons and holes of  $TiO_2$  in methane oxidation, as shown in Figure 12a [133]. Under

light irradiation, the absorption signal across the NIR region is dominated by photoexcited electrons, while the absorption in the visible region is related to the photoexcited holes. The spectrum under Ar atmosphere was used as a reference. When air was introduced, photogenerated electrons were quenched by  $O_2$ . Thus, the number of photogenerated electrons was significantly reduced, while holes accumulated at the valence band of  $TiO_2$ . Therefore, a decrease in the absorption of NIR regions was detected (Figure 12b). When only methane was used, an increase in the absorption was observed, which provided direct evidence for the fact that the initial step of methane activation over  $TiO_2$  involved oxidation by photoexcited holes (Figure 12c). Moreover, when both methane and air were introduced, a reduction of both the absorption at the visible and NIR region was ob-

tained (Figure 12d). Similarly, photoinduced electrons in the conduction band of  $\text{TiO}_2$  were observed by IR spectroscopy at the wavenumber from  $3500$  to  $1700\text{ cm}^{-1}$  [118]. Under Ar atmosphere, the signal of photoinduced electrons firstly increased and then followed a slow decay with continuous light irradiation. When Ar was replaced by  $\text{CH}_4$ , the strong signal resulted from the photoelectrons was maintained for as long as 250 min. This was because photoholes were quenched by  $\text{CH}_4$ , and electrons accumulated at the conduction band of  $\text{TiO}_2$ .

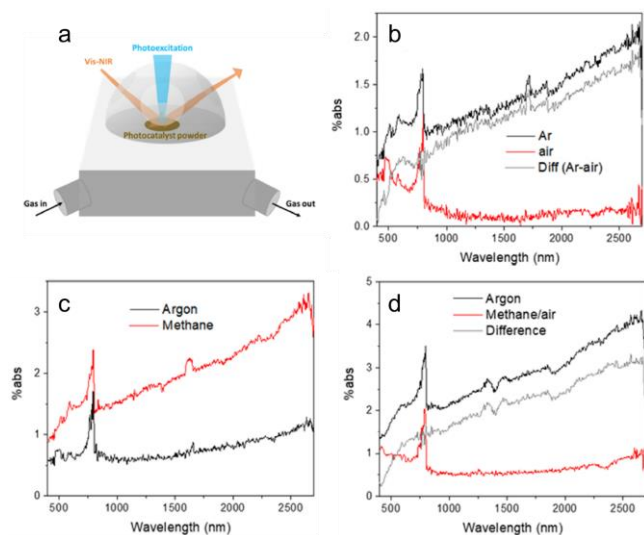


**Figure 12.** In situ observation of charge behaviours in methane oxidation via UV-Vis-NIR spectroscopy; (a) Reaction setup; Absorption in the presence of (b) Ar and air, (c) Ar and  $\text{CH}_4$ , and (d) Ar and  $\text{CH}_4$ +air. Reprinted from ref. [133]. Copyright 2021 American Chemical Society (colour online).

Near edge X-ray absorption fine structure (NEXAFS) spectroscopy can be a powerful tool to probe the electronic structure of solid catalysts. Recently, NEXAFS was applied to investigate the charge separation and migration in  $\text{TiO}_2$  during photocatalytic methane oxidation [118]. As shown in Figure 13 a-c, the Ti L-edge and O K-edge spectra of  $\text{TiO}_2$  photocatalysts with exposed  $\{001\}$ ,  $\{100\}$  and  $\{101\}$  facets were examined under dark and light irradiation conditions. The O K-edge signals were resulted from the electron transition from the O 1s to O 2p orbital, while Ti L-edge signals originated from the electron transition from Ti 2p to Ti 3d orbital. Upon UV-light irradiation, electrons were excited from the O 2p to Ti 3d orbitals, resulting in more unoccupied O 2p and less unoccupied Ti 3d orbitals. Therefore, a decrease in the Ti L-edge and an increase in the O K-edge were detected (Figure 13d). The change of Ti L-edge and O K-edge signals should be the same when the charge generation, separation and recombination all occurred locally at the surface of the catalysts. However, the  $\Delta I_{\text{O K-edge}}/\Delta I_{\text{Ti L-edge}}$  ratios differed from the three  $\text{TiO}_2$  catalysts, as shown in Fig. 12e. A high  $\Delta I_{\text{O K-edge}}/\Delta I_{\text{Ti L-edge}}$  ratio of 2.08 over the  $\text{TiO}_2\{-001\}$  catalyst suggested an efficient bulk to surface

immigration of holes and surface to bulk immigration of electron, leading to strongly photoexcited holes-enriched surface, which was beneficial for  $\text{CH}_4$  activation (Fig. 12f).

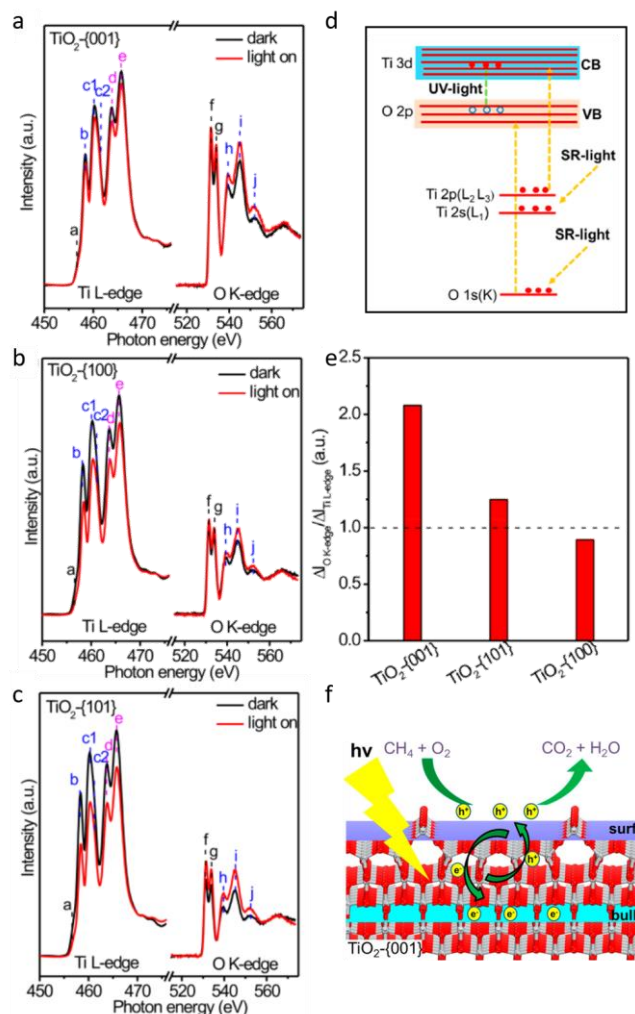


**Figure 13.** The Ti L-edge and O K-edge NEXAFS spectra of (a)  $\text{TiO}_2\{-001\}$ , (b)  $\text{TiO}_2\{-100\}$  and (c)  $\text{TiO}_2\{-101\}$  under dark and UV irradiation conditions; (d) Schematic illustration of NEXAFS working principle of  $\text{TiO}_2$  upon UV light illumination; (e)  $\Delta I_{\text{O K-edge}}/\Delta I_{\text{Ti L-edge}}$  ratio of  $\text{TiO}_2\{-001\}$ ,  $\text{TiO}_2\{-100\}$  and  $\text{TiO}_2\{-101\}$ ; (f) Schematic illustration showing the bulk-surface change immigration in  $\text{TiO}_2\{-001\}$  catalyst. Reprinted from ref. [118]. Copyright 2022 American Chemical Society (colour online).

Surface chemistry plays the same important role as photophysics in photocatalytic methane oxidation. The main surface chemistry-related processes in photocatalytic methane conversion include reactant adsorption, reactant activation, radical generation and reaction, product formation and desorption. The adsorption of reactants on the surface of catalysts is the first step of the whole reaction and can have a significant effect on the performance of the photocatalyst. Temperature programmed desorption (TPD) has been widely used in thermocatalysis to study the adsorption of reactants and intermediates on the catalyst surface. Nev-

ertheless, this has hardly been used in photocatalytic methane oxidation. Pure SrTiO<sub>3</sub> prepared either by hydrothermal method or solid-state reaction method was not active in methane oxidation [30]. However, SrTiO<sub>3</sub> prepared via a sol-gel method was capable of methane activation. It was found that SrCO<sub>3</sub> introduced on SrTiO<sub>3</sub> during the sol-gel process could greatly modify the methane adsorption on SrTiO<sub>3</sub>, as evidenced by CH<sub>4</sub>-TPD. O<sub>2</sub>-TPD could characterise the O<sub>2</sub> adsorption and activation capability of solid catalysts [125]. Au modified ZnO and ZnO/TiO<sub>2</sub> photocatalysts used for oxidative coupling of methane were measured by O<sub>2</sub>-TPD to prove the effect of Au on improving oxygen adsorption and activation [114].

The activation of adsorbed CH<sub>4</sub> and O<sub>2</sub> produces corresponding radicals for later reactions in photocatalytic methane oxidation. Methyl radicals ( $\cdot\text{CH}_3$ ) are the most important radicals and intermediates formed in methane conversion reactions. Observation of  $\cdot\text{CH}_3$  radicals via electron paramagnetic resonance (EPR) has been reported in other photocatalytic methane conversion reactions, such as partial oxidation of methane for C<sub>1</sub> oxygenates production and non-oxidative coupling of methane [134,135]. In situ Raman spectroscopy was also used to detect the formation of methyl radicals in photoelectrochemical methane conversion to CO [136]. However,  $\cdot\text{CH}_3$  has not been reported in photocatalytic methane complete oxidation. Reactive oxygen species (e.g.,  $\cdot\text{O}^{2-}$  and  $\cdot\text{OOH}$  radicals) are the products of oxygen reduction by photogenerated electrons, which is not only beneficial for charge separation but also facilitates methane oxidation in photocatalytic methane combustion. ROS have been frequently detected by ex situ EPR radical trapping experiments in various photocatalytic methane conversion reactions [137,138]. Very recently, the direct observation of ROS by in situ EPR in photocatalytic methane oxidation has been achieved at -153 °C (Figure 14a) [114]. Pt and Au-loaded ZnO/TiO<sub>2</sub> photocatalysts were firstly treated under vacuum at 150 °C to remove surface adsorbed oxygen species. Then, the catalysts were exposed to oxygen and tested by EPR under dark and UV irradiation. The two signals at  $g = 1.959$  and  $2.000$  originated from oxygen vacancies and Zn<sup>+</sup> of the catalysts, respectively. New signals at  $g$  value of 2.020 to 2.033 were observed after UV irradiation, which were ascribed to the oxygen species formed by the reaction between the catalyst surface and oxygen gas. The control experiment showed that this signal was not visible under vacuum conditions. It was noted that Pt as a co-catalyst could promote the formation of ROS better than Au. Therefore, the product obtained over Pt-ZnO/TiO<sub>2</sub> was solely CO<sub>2</sub>, while Au-ZnO/TiO<sub>2</sub> could selectively produce C<sub>2</sub>H<sub>6</sub>. Moreover, when CH<sub>4</sub> and O<sub>2</sub> were both introduced, the ROS signal was decreased compared to that in the absence of CH<sub>4</sub>. This indicated that ROS as an important radical was consumed in methane oxidation. The high ability of Pt as a co-catalyst in the production of

ROS was further proved by in situ ATR-IR spectroscopy [114]. The IR band at 1128 cm<sup>-1</sup>, which was ascribed to  $\cdot\text{O}^{2-}$  radicals [139], became visible and stronger after light irradiation (Figure 14b). In contrast, this signal was hardly visible when Au was used as the co-catalyst for methane oxidation.

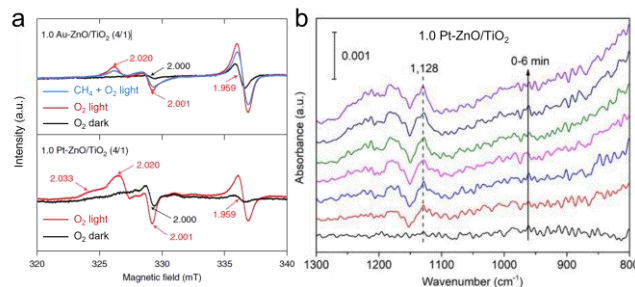


**Figure 14.** In situ observation of ROS: (a) In situ EPR spectra of Au and Pt modified ZnO/TiO<sub>2</sub> photocatalyst; (b) In situ ATR-IR spectra of Pt modified ZnO/TiO<sub>2</sub>. Reprinted from ref. [114]. Copyright 2021 Springer Nature (colour online).

IR spectroscopy is a sensitive probe to observe organic compounds and H<sub>2</sub>O. Thus, DRIFTS allows the detection of the intermediates formed on the surface of catalysts to reveal the reaction pathway and mechanisms of photocatalytic methane oxidation [140]. When using Ag-ZnO as the photocatalyst, the bands at 1305 and 3015 cm<sup>-1</sup> originated from methane became weaker with prolonged irradiation time (Figure 15a) [123]. In contrast, the signals at 2360 cm<sup>-1</sup>, which was resulted from the asymmetric stretch of C=O, kept increasing. The bands at 1625 and 3400 cm<sup>-1</sup> were the results of  $\delta$  (HOH) and  $\nu$  (HOH) vibrations of chemisorbed water. The only intermediates observed were  $\cdot\text{CHO}$  species, which were featured by the IR band at 1425 cm<sup>-1</sup>. The current result obtained from DRIFTS observations only showed the evolution of products and reactants, and thus could not provide a complete view of the catalytic process. Later, Pt-ZnO/TiO<sub>2</sub>, which selectively produced CO<sub>2</sub> from photocatalytic methane oxidation, was tested in an in situ IR spectrometre [114]. As shown in Figure 15b, the band at 2880 cm<sup>-1</sup> was originated from the stretching vibration of C-H bond in the adsorbed  $\cdot\text{OCH}_3$  species, which was an important species for CO<sub>2</sub> production from methane oxidation. Similarly, HCHO was observed at the wavenumber of 1277 cm<sup>-1</sup>. Moreover, HCOO $\cdot$  was also detected, evidenced by the stretching vibrations at 1313, 1375 and 1594 cm<sup>-1</sup>. The two bands at 2330 and 2362 cm<sup>-1</sup> were resulted from gaseous CO<sub>2</sub> produced by methane oxidation. Very recently, the evolution of these intermediates over time in photocatalytic methane oxidation by TiO<sub>2</sub> catalyst was studied using in situ DRIFTS [118]. The detected species included  $\cdot\text{OCH}_3$ , HCO $\cdot$ , HCHO and HCOO $\cdot$  species, as displayed in Figure 15c. The signals for  $\cdot\text{OCH}_3$  were relatively stable, indicating the formation rate and consumption rate of this intermediate

were similar. The intensity of bands from  $\text{HCO}\cdot$  and  $\text{HCHO}$  firstly increased and then decreased quickly, indicating the oxidation of  $\text{HCO}\cdot$  and  $\text{HCHO}$  was much faster than its formation. Finally, the accumulation of  $\text{HCOO}\cdot$  species on the surface of  $\text{TiO}_2$  was observed, indicating that the oxidation of  $\text{HCOO}\cdot$  was the rate limiting step among the whole intermediate reactions. Based on the above, it can be proposed that the photocatalytic methane oxidation process followed a  $\text{CH}_4 \rightarrow \cdot\text{CH}_3 \rightarrow \cdot\text{OCH}_3 \rightarrow \text{HCHO} \rightarrow \text{HCOOH} \rightarrow \text{CO}_2$  route (Figure 15d).

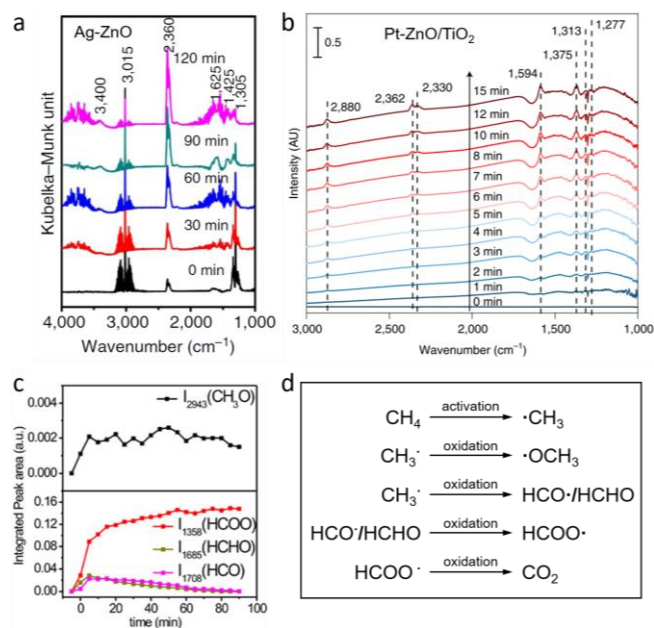


**Figure 15.** (a) In situ IR spectra of methane photocatalytic oxidation over  $\text{Ag-ZnO}$ . Reprinted from ref. [123]. Copyright 2016 Springer Nature (colour online). (b) In situ IR spectra of  $\text{Pt-ZnO/TiO}_2$  in photocatalytic methane oxidation. Reprinted from ref. [114]. Copyright 2021 Springer Nature (colour online). (c) Evolution of intermediates on  $\text{TiO}_2$  in photocatalytic methane oxidation observed by in situ IR. Reprinted from ref. [118]. Copyright 2022 American Chemical Society (colour online). (d) Proposed reaction pathway for photocatalytic methane oxidation.

Desorption of  $\text{CO}_2$ , which cleans the surface of the catalyst, is the final step of photocatalytic methane oxidation and has been hardly considered. Up to now,  $\text{CO}_2$  adsorption was only studied when  $\text{SrCO}_3$  was loaded on  $\text{SrTiO}_3$  as a co-catalyst. In situ DRIFTS and TPD-MS were used to detect the adsorbed  $\text{CO}_2$  on the surface of the catalyst [30]. It was found that basic materials including  $\text{MgO}$ ,  $\text{CaO}$ ,  $\text{BaO}$ ,  $\text{CuO}$  and  $\text{Fe}_2\text{O}_3$ , displayed a high  $\text{CO}_2$  adsorption capacity. Although they were capable of methane adsorption, the surface would be saturated by  $\text{CO}_2$  in the reaction. Thus, the adsorption sites for reactants are blocked, and methane oxidation could hardly take place. In contrast,  $\text{CO}_2$  could not be adsorbed on  $\text{SrCO}_3$  surface, indicating that the produced  $\text{CO}_2$  could readily desorb from the catalyst, facilitating later cycles for methane oxidation. Apart from IR and TPD, DFT calculation can help to simulate the adsorption of  $\text{CO}_2$  on

different surfaces, which can guide the design of methane oxidation photocatalysts. However, this was only reported in thermocatalysis [141].

## 4 Summary and outlooks

Methane oxidation via heterogeneous catalysis (including both thermocatalysis and photocatalysis) holds great potential in alleviating the environmental issues caused by the emission of methane into the atmosphere. The so far used and studied catalysts are mainly focused on noble-metal-based materials (e.g., Pd, Pt, etc.) working at relatively high temperatures. The main aim should be to develop cost-effective catalysts and reduce reaction temperatures. The developed thermocatalysts, including both noble-metal- and transition-metal-oxide-based materials have been summarised. Fundamental studies of the catalytic mechanisms of thermocatalytic methane oxidation using advanced spectroscopies and microscopies were also discussed. Photocatalysis, which is a new technology that operates under mild conditions, could be an alternative to thermocatalysis in methane oxidation. Several UV-responsive photocatalysts (e.g.,  $\text{TiO}_2$ ,  $\text{ZnO}$  and  $\text{SrTiO}_3$ ) were proved active for methane oxidation. Some pioneering fundamental studies were also attempted to reveal the photophysics and surface chemistry involved in the photocatalytic methane oxidation process.

Thermocatalytic methane oxidation, which requires high temperature to drive the reaction, has been studied for decades and substantial achievements have been acquired. The high methane conversion rate via thermocatalysis is the most attractive feature. The supported Pd-Pt-Ru catalyst, with an operational temperature of  $400\text{ }^\circ\text{C}$  has been commercially applied in catalytic converters for vehicle exhaust treatment, showing an efficiency of nearly 100%. The noble metals in deactivated catalytic converters can also be recovered and re-used. Despite this, the development of active noble-metal-free catalysts and significant reduction of the noble metal content in the catalyst are preferred due to their high demand. Another issue is the catalyst deactivation due to metal sintering and the poisoning of catalysts by humid,  $\text{SO}_2$  and  $\text{CO}_2$ , which greatly limits the long-term durability and practical application of the catalytic methane oxidation system. More importantly, it is encouraged to test the performance of catalysts under near-real application conditions (lean methane mixed with water,  $\text{CO}_2$  and  $\text{NO}_x$ ,  $\text{SO}_2$ , etc.) to give a complete view of the catalyst in operational conditions. The working temperature of most existing catalysts is still high ( $400\text{ }^\circ\text{C}$  or higher). Lowering the temperature (e.g.,

to  $< 300$  °C) can greatly extend the practical application of the current methane oxidation technology. Fundamental understanding of thermocatalytic methane oxidation is not studied as intensively as other methane conversion reactions (e.g., non-oxidative coupling of methane, partial oxidation of methane). It is essential to track the reaction pathway by monitoring the formation, accumulation and consumption of radicals and intermediates during the reaction to determine the rate-limiting step, as fully understanding the catalytic mechanism can provide important guidance for the development of thermocatalysts. Overall, future studies for thermocatalytic methane oxidation should pay more attention to cost-effective catalysts that work at relatively low temperatures. Furthermore, the catalyst durability and anti-poison capability (e.g., against  $\text{H}_2\text{O}$ ,  $\text{SO}_2$ , etc.) are also important factors to be considered. The fundamental investigations related to the catalyst-support interaction and methane activation could provide meaningful guidance to improve the catalyst activity. From the engineering aspect of view, careful design of the reaction system to prolong the detention time of reactants on the catalyst surface can also improve the efficiency of the catalytic process.

Photocatalysis, which uses the energy of photons instead of heat to drive chemical reactions, has shown its potential in methane oxidation, although the research is only at very early stages. Photocatalytic methane oxidation is usually operated at room temperature and under atmospheric pressure. The operation conditions are substantially more moderate than traditional thermocatalysis. Moreover, the inexhaustible solar energy, instead of heat energy usually obtained from burning fossil fuels, could be used in photocatalysis, which makes the process not only economically but also environmentally preferable. Thus, more attention should be paid to methane oxidation via this green process. The major concerns include the following. Firstly, the performance of methane oxidation photocatalysts is considerably lower than thermocatalysis at present. In most cases, a noticeable methane conversion could be achieved only when using dry methane in the presence of pure air. Secondly, the most studied photocatalysts for methane oxidation are ZnO and  $\text{TiO}_2$ , which are both UV-responsive photocatalysts. Broadening the absorption range of catalysts into the visible region is essential, as such natural sunlight could be efficiently used when photocatalytic methane oxidation is put into practical applications. Thirdly, the performance test should be standardised to allow a meaningful

comparison between different publications. The reaction condition is also suggested to reflect the real application. For instance, the ratio of methane to air, the effect of water vapour, CO,  $\text{SO}_2$  and  $\text{NO}_x$  on the performance of the catalyst should be involved. The long-term stability test for up to hundreds and thousands of hours for the photocatalyst is essential though most of the currently reported catalysts were only tested for less than 10 hours. Moreover, the reactors used in photocatalytic methane oxidation are mostly batch reactors, which show moderate efficiency, and low potential in industrial applications. Thus, flow reactors should be investigated. Lastly, the study of the photophysics and surface chemistry in photocatalytic methane oxidation, especially using the established technologies in thermocatalysis could provide important guidance for the development of this new technology. In future investigation, the main aim should be to develop efficient, durable and visible-responsive catalysts via co-catalyst loading, and the formation of heterostructures, particularly Z-scheme catalysts, as this may offer a potential solution for the removal of atmospheric methane. Polymer semiconductors are an important group of photocatalysts that can be potentially used for methane removal since the surface and band potentials could be tailored specially for methane oxidation. In the reaction engineering aspect, the application of flow reactors can realise continuous methane oxidation. The inner structure of the reactor should be carefully designed to achieve efficient mass transfer. Another method to improve the performance of the photocatalytic process is by the design of high-efficiency light sources and/or increasing the irradiation area to increase energy input in photocatalysis. For instance, panel reactors at the scale of  $100 \text{ m}^2$  were manufactured for water splitting using sunlight.[142] Although the main energy source in photocatalysis is photons, the overall performance of the catalytic process can be significantly improved with mild heating ( $100\text{-}200$  °C). Thus, photocatalytic reactors could be equipped with temperature control units. The delicate design of the reaction system can considerably improve the efficiency of the catalytic process as well as make the process potentially more applicable.

The catalytic oxidation of methane is drawing increasing attention and addresses important environmental concerns and energy issues. However, the current achievement could and still needs to be improved, not only to mention new catalysts but also catalytic systems. Much is required to be further studied in catalyst design, reaction engineering and fundamental mechanisms, especially for photocatalytic me-

thane oxidation. With continuous efforts and research devoted, industrialised efficient methane removal process under milder conditions could be expected to mitigate the environmental issues caused by methane emission.

**Acknowledgments** All authors are thankful for UK EPSRC (EP/S018204/2), Royal Society Newton Advanced Fellowship grant (NAF/R1\191163), and Royal Society Leverhulme Trust Senior Research Fellowship (SRF/R1\21000153). C.W. and Y. X. acknowledge the UCL Dean's prize and China CSC scholarship.

**Conflict of interest** The authors declare that they have no conflict of interest.

- Holmes CD, Prather MJ, Søvdø OA, Myhre G. *Atmos Chem Phys*, 2013, 13: 285–302
- Dietrich Oesté F, De Richter R, Ming T, Caillol S. *Earth Syst Dyn*, 2017, 8: 1–54
- Smith P, Goulding KW, Smith KA, Powlson DS, Smith JU, Falloon P, Coleman K. *Nutr Cycl Agroecosystems*, 2001, 60: 237–252
- Majdinasab A, Yuan Q. *Ecol Eng*, 2017, 104: 116–130
- Bae JS, Su S, Yu XX. *Ind Eng Chem Res*, 2019, 58: 21700–21707
- Wang W, Ren J, Li X, Li H, Li D, Li H, Song Y. *Sci Rep*, 2020, 10: 7276
- Kulkarni MR, Sardesai CR. *J Energy Eng*, 2002, 128: 1–12
- Furukawa H, Ko N, Go YB, Aratani N, Choi SB, Choi E, Yazaydin AO, Snurr RQ, O'Keefe M, Kim J, Yaghi OM. *Science (80- )*, 2010, 329: 424–428
- Mendoza-Cortes JL, Pascal TA, Goddard WA. *J Phys Chem A*, 2011, 115: 13852–13857
- Zabielska K, Aleksandrak T, Gabruś E. *Chem Process Eng - Inz Chem i Proces*, 2018, 39: 309–321
- Conditions T. *J Am Chem Soc*, 1927, 49: 1454–1460
- Murata K, Mahara Y, Ohyama J, Yamamoto Y, Arai S, Satsuma A. *Angew Chemie - Int Ed*, 2017, 56: 15993–15997
- Danielis M, Betancourt LE, Orozco I, Divins NJ, Llorca J, Rodríguez JA, Senanayake SD, Colussi S, Trovarelli A. *Appl Catal B Environ*, 2021, 282: 119567
- Epling WS, Hoflund GB. *J Catal*, 1999, 182: 5–12
- Chen J, Buchanan T, Walker EA, Toops TJ, Li Z, Kunal P, Kyriakidou EA. *ACS Catal*, 2021, 11: 9345–9354
- Wang H, Chen C, Zhang Y, Peng L, Ma S, Yang T, Guo H, Zhang Z, Su DS, Zhang J. *Nat Commun*, 2015, 6: 2–7
- Arandiyán H, Dai H, Deng J, Liu Y, Bai B, Wang Y, Li X, Xie S, Li J. *J Catal*, 2013, 307: 327–339
- Bao D, Zhang Q, Meng FL, Zhong HX, Shi MM, Zhang Y, Yan JM, Jiang Q, Zhang XB. *Adv Mater*, 2017, 29
- Nitopi S, Bertheussen E, Scott SB, Liu X, Engstfeld AK, Horch S, Seger B, Stephens IEL, Chan K, Hahn C, Nørskov JK, Jaramillo TF, Chorkendorff I. *Chem Rev*, 2019, 119: 7610–7672
- Chen S, Takata T, Domen K. *Nat Rev Mater*, 2017, 2: 17050
- Xie J, Jin R, Li A, Bi Y, Ruan Q, Deng Y, Zhang Y, Yao S, Sankar G, Ma D, Tang J. *Nat Catal*, 2018, 1: 889–896
- Gong Z, Luo L, Wang C, Tang J. *Sol RRL*, 2022, 6: 2200335
- Luo L, Fu L, Liu H, Xu Y, Xing J, Chang CR, Yang DY, Tang J. *Nat Commun*, 2022, 13
- Luo L, Gong Z, Xu Y, Ma J, Liu H, Xing J, Tang J. *J Am Chem Soc*, 2022, 144: 740–750
- Kaliaguine SL, Shelimov BN, Kazansky VB. *J Catal*, 1978, 55: 384–393
- Zhang W, Yu Y, Yi Z. *J Mater Sci*, 2017, 52: 5106–5116
- Zhu X, Liang X, Wang P, Dai Y, Huang B. *Appl Surf Sci*, 2018, 456: 493–500
- Li Z, Pan X, Yi Z. *J Mater Chem A*, 2019, 7: 469–475
- Wang F, Liang X, Wang P, Zhang Q, Tong F, Wang Z, Liu Y, Zheng Z, Cheng H, Dai Y, Huang B. *J Environ Chem Eng*, 2021, 9: 106435
- Pan X, Chen X, Yi Z. *Phys Chem Chem Phys*, 2016, 18: 31400–31409
- Schwach P, Pan X, Bao X. *Chem Rev*, 2017, 117: 8497–8520
- Wen W, Che JW, Wu JM, Kobayashi H, Pan Y, Wen W, Dai YH, Huang W, Fu C, Zhou Q, Lu GL, Tian H, Liu J, Yang P, Chen X, Sun TL, Fan J. *ACS Catal*, 2022, 12: 7037–7045
- Joo L, David T. *Fuel Process Technol*, 1995, 42: 339–359
- Li X, Wang C, Tang J. *Nat Rev Mater*, 2022, 7: 617–632
- Burch R, Urbano FJ, Loader PK. *Appl Catal A, Gen*, 1995, 123: 173–184
- Kleinschmidt O, Hesse D. *Can J Chem Eng*, 2002, 80: 71–78
- Peat S, Wales N. *Nature*, 1968, 217: 1252–1253
- Du J, Zhao D, Wang C, Zhao Y, Li H, Luo Y. *Catal Sci Technol*, 2020, 10: 7875–7882
- Kumsung W, Chareonpanich M, Kongkachuichay P, Senkan S, Seubsai A. *Catal Commun*, 2018, 110: 83–87
- Grunwaldt JD, Vegten N Van, Baiker A. *Chem Commun*, 2007, 4635–4637
- Grisel RJH, Kooyman PJ, Nieuwenhuys BE. *J Catal*, 2000, 191: 430–437
- Pecchi G, Reyes P, Gómez R, López T, Fierro JLG. *Appl Catal B Environ*, 1998, 17: L7–L18
- Wang Z, Khalid O, Wang W, Wang Y, Weber T, Spriewald Luciano A, Zhan W, Smarsly BM, Over H. *Catal Sci Technol*, 2021, 11: 6839–6853
- Chen J, Wang X, Zhang L, Rui Z. *Appl Catal B Environ*, 2021, 297: 120410
- Chen J, Zhong J, Wu Y, Hu W, Qu P, Xiao X, Zhang G, Liu X, Jiao Y, Zhong L, Chen Y. *ACS Catal*, 2020, 10: 10339–10349
- Ma J, Lou Y, Cai Y, Zhao Z, Wang L, Zhan W, Guo Y, Guo Y. *Catal Sci Technol*, 2018, 8: 2567–2577
- Duan Q, Zhang C, Sun S, Pan Y, Zhou X, Liu Y, Chen K, Li C, Wang X, Li W. *J Mater Chem A*, 2020, 8: 7395–7404
- Yang X, Li Q, Lu E, Wang Z, Gong X, Yu Z, Guo Y, Wang L, Guo Y, Zhan W, Zhang J, Dai S. *Nat Commun*, 2019, 10: 1–9
- Sekizawa K, Widjaja H, Maeda S, Ozawa Y, Eguchi K. *Appl Catal A Gen*, 2000, 200: 211–217
- Tang M, Li S, Chen S, Ou Y, Hiroaki M, Yuan W, Zhu B, Yang H, Gao Y, Zhang Z, Wang Y. *Angew Chemie - Int Ed*, 2021, 60: 22339–22344
- Li T, Beck A, Krumeich F, Artiglia L, Ghosal MK, Roger M,

- Ferri D, Kröcher O, Sushkevich V, Safonova O V., van Bokhoven JA. *ACS Catal*, 2021, 11: 7371–7382
52. Corro G, Cano C, Fierro JLG. *J Mol Catal A Chem*, 2010, 315: 35–42
53. Peng H, Dong T, Yang S, Chen H, Yang Z, Liu W, He C, Wu P, Tian J, Peng Y, Chu X, Wu D, An T, Wang Y, Dai S. *Nat Commun*, 2022, 13: 1–10
54. Monai M, Montini T, Gorte RJ, Fornasiero P. *Eur J Inorg Chem*, 2018, 2018: 2884–2893
55. Lyubovsky M, Pfefferle L. *Appl Catal A Gen*, 1998, 173: 107–119
56. Datye AK, Bravo J, Nelson TR, Atanasova P, Lyubovsky M, Pfefferle L. *Appl Catal A Gen*, 2000, 198: 179–196
57. Peng H, Rao C, Zhang N, Wang X, Liu W, Mao W, Han L, Zhang P, Dai S. *Angew Chemie - Int Ed*, 2018, 57: 8953–8957
58. Toso A, Colussi S, Padigapaty S, de Leitenburg C, Trovarelli A. *Appl Catal B Environ*, 2018, 230: 237–245
59. Xiao Y, Li J, Wang C, Zhong F, Zheng Y, Jiang L. *Catal Sci Technol*, 2021, 11: 836–845
60. Burch R, Urbano FJ. *Appl Catal A, Gen*, 1995, 124: 121–138
61. Friberg I, Sadokhina N, Olsson L. *Appl Catal B Environ*, 2018, 231: 242–250
62. Hong E, Kim C, Lim DH, Cho HJ, Shin CH. *Appl Catal B Environ*, 2018, 232: 544–552
63. Xiao LH, Sun KP, Xu XL, Li XN. *Catal Commun*, 2005, 6: 796–801
64. Kyriakidou EA, Chen J, Giewont K, Walker EA, Lee J, Niu Y. *ACS Catal*, 2021, 11: 13066–13076
65. Murthy PR, Zhang JC, Li WZ. *Catal Sci Technol*, 2021, 11: 3609–3618
66. Petrov AW, Ferri D, Krumeich F, Nachtegaal M, Van Bokhoven JA, Kröcher O. *Nat Commun*, 2018, 9: 2545
67. Descorme C, Gélin P, Lécuyer C, Primet M. *Appl Catal B Environ*, 1997, 13: 185–195
68. Wang T, Qiu L, Li H, Zhang C, Sun Y, Xi S, Ge J, Xu ZJ, Wang C. *J Catal*, 2021, 404: 400–410
69. Yang J, Peng M, Ren G, Qi H, Zhou X, Xu J, Deng F, Chen Z, Zhang J, Liu K, Pan X, Liu W, Su Y, Li W, Qiao B, Ma D, Zhang T. *Angew Chemie - Int Ed*, 2020, 59: 18522–18526
70. Colussi S, Trovarelli A, Vesselli E, Baraldi A, Comelli G, Groppi G, Llorca J. *Appl Catal A Gen*, 2010, 390: 1–10
71. Chen Y, Lin J, Chen X, Fan S, Zheng Y. *Catal Sci Technol*, 2021, 11: 152–161
72. Persson K, Ersson A, Jansson K, Iverlund N, Järås S. *J Catal*, 2005, 231: 139–150
73. Wang Y, Arandiyán H, Scott J, Akia M, Dai H, Deng J, Aguey-Zinsou KF, Amal R. *ACS Catal*, 2016, 6: 6935–6947
74. Li W, Liu D, Feng X, Zhang Z, Jin X, Zhang Y. *Adv Energy Mater*, 2019, 9: 1–9
75. Jang EJ, Lee J, Oh DG, Kwak JH. *ACS Catal*, 2021, 11: 5894–5905
76. Xiong H, Kunwar D, Jiang D, García-Vargas CE, Li H, Du C, Canning G, Pereira-Hernandez XI, Wan Q, Lin S, Purdy SC, Miller JT, Leung K, Chou SS, Brongersma HH, ter Veen R, Huang J, Guo H, Wang Y, Datye AK. *Nat Catal*, 2021, 4: 830–839
77. Cargnello M, Delgado Jaén JJ, Hernández Garrido JC, Bakhmutsky K, Montini T, Calvino Gámez JJ, Gorte RJ, Fornasiero P. *Science (80-)*, 2012, 337: 713–717
78. Li T, Yao Y, Huang Z, Xie P, Liu Z, Yang M, Gao J, Zeng K, Brozena AH, Pastel G, Jiao M, Dong Q, Dai J, Li S, Zong H, Chi M, Luo J, Mo Y, Wang G, Wang C, Shahbazian-Yassar R, Hu L. *Nat Catal*, 2021, 4: 62–70
79. Beck IE, Bukhtiyarov VI, Pakharukov IY, Zaikovskiy VI, Krivtsov V V., Parmon VN. *J Catal*, 2009, 268: 60–67
80. Machocki A, Ioannides T, Stasinska B, Gac W, Avgouropoulos G, Delimaris D, Grzegorzczak W, Pasieczna S. *J Catal*, 2004, 227: 282–296
81. Corro G, Torralba R, Pal U, Olivares-Xometl O, Fierro JLG. *J Phys Chem C*, 2019, 123: 2882–2893
82. Yu Q, Liu C, Li X, Wang C, Wang X, Cao H, Zhao M, Wu G, Su W, Ma T, Zhang J, Bao H, Wang J, Ding B, He M, Yamauchi Y, Zhao XS. *Appl Catal B Environ*, 2020, 269: 118757
83. Hu L, Peng Q, Li Y. *J Am Chem Soc*, 2008, 130: 16136–16137
84. Yang KR, Batista VS, Pfefferle LD, He Y, Guo F, Heinlein JA, Bamonte SM, Fee JJ, Hu S, Suib SL, Haller GL. *J Am Chem Soc*, 2020, 142: 17119–17130
85. Hao YJ, Tian LG, Duan E, Liu J, Qi TY, Kong WQ, Qi XH, Liu X, Liu Y, Zhao J, Li FT. *ACS Appl Mater Interfaces*, 2020, 12: 21761–21771
86. Fuentes RO, Acuña LM, Leyva AG, Baker RT, Pan H, Chen X, Delgado-Jaén JJ. *J Mater Chem A*, 2018, 6: 7488–7499
87. Oh SC, Xu J, Tran DT, Liu B, Liu D. *ACS Catal*, 2018, 8: 4493–4507
88. Wang Y, Ren J, Wang Y, Zhang F, Liu X, Guo Y, Lu G. *J Phys Chem C*, 2008, 112: 15293–15298
89. Spretz R, Marchetti SG, Ulla MA, Lombardo EA. *J Catal*, 2000, 194: 167–174
90. Zhang Z, Li J, Yi T, Sun L, Zhang Y, Hu X, Cui W, Yang X. *Chinese J Catal*, 2018, 39: 1228–1239
91. Fan X, Li L, Jing F, Li J, Chu W. *Fuel*, 2018, 225: 588–595
92. Tao FF, Shan JJ, Nguyen L, Wang Z, Zhang S, Zhang L, Wu Z, Huang W, Zeng S, Hu P. *Nat Commun*, 2015, 6: 7798
93. Dai Y, Kumar VP, Zhu C, Wang H, Smith KJ, Wolf MO, MacLachlan MJ. *Adv Funct Mater*, 2019, 29
94. Yang N, Ni S, Sun Y, Zhu Y. *Mol Catal*, 2018, 452: 28–35
95. Li Y, Armor JN. *Appl Catal B, Environ*, 1994, 3: 275–282
96. Cullis CF, Nevell TG, Trimm DL. *J Chem Soc Faraday Trans 1 Phys Chem Condens Phases*, 1972, 68: 1406–1412
97. Ciuparu D, Pfefferle L. *Appl Catal A Gen*, 2001, 209: 415–428
98. Gao M, Gong Z, Weng X, Shang W, Chai Y, Dai W, Wu G, Guan N, Li L. *Chinese J Catal*, 2021, 42: 1689–1699
99. Wilburn MS, Epling WS. *ACS Catal*, 2019, 9: 640–648
100. Mowery DL, Graboski MS, Ohno TR, McCormick RL. *Appl Catal B Environ*, 1999, 21: 157–169
101. Mowery DL, McCormick RL. *Appl Catal B Environ*, 2001, 34: 287–297
102. Yang J, Guo Y. *Chinese Chem Lett*, 2018, 29: 252–260
103. Monai M, Montini T, Melchionna M, Duchoň T, Kúš P, Chen C, Tsud N, Nasi L, Prince KC, Veltruská K, Matolín V, Khader MM, Gorte RJ, Fornasiero P. *Appl Catal B Environ*, 2017, 202: 72–83

104. Gabasch H, Hayek K, Klötzer B, Unterberger W, Kleimenov E, Teschner D, Zafeiratos S, Hävecker M, Knop-Gericke A, Schlögl R, Aszalos-Kiss B, Zemlyanov D. *J Phys Chem C*, 2007, 111: 7957–7962
105. Han YF, Ramesh K, Chen L, Widjaja E, Chilukoti S, Chen F. *J Phys Chem C*, 2007, 111: 2830–2833
106. Baylet A, Marécot P, Duprez D, Castellazzi P, Groppi G, Forzatti P. *Phys Chem Chem Phys*, 2011, 13: 4607–4613
107. Wang L, Wang L, Meng X, Xiao FS. *Adv Mater*, 2019, 31
108. Driscoll DJ, Martir W, Wang JX, Lunsford JH. *J Am Chem Soc*, 1985, 107: 58–63
109. Stotz H, Maier L, Boubnov A, Gremminger AT, Grunwaldt JD, Deutschmann O. *J Catal*, 2019, 370: 152–175
110. Martin R, Lee CJ, Mehar V, Kim M, Asthagiri A, Weaver JF. *ACS Catal*, 2022, 12: 2840–2853
111. Feng X, Liu D, Yan B, Shao M, Hao Z, Yuan G, Yu H, Zhang Y. *Angew Chemie - Int Ed*, 2021, 60: 18552–18556
112. Krishna V, Kamble VS, Selvam P, Gupta NM. *Catal Letters*, 2004, 98: 113–116
113. Yu X, De Waele V, Löfberg A, Ordonsky V, Khodakov AY. *Nat Commun*, 2019, 10: 1–10
114. Song S, Song H, Li L, Wang S, Chu W, Peng K, Meng X, Wang Q, Deng B, Liu Q, Wang Z, Weng Y, Hu H, Lin H, Kako T, Ye J. *Nat Catal*, 2021, 4: 1032–1042
115. Yu X, Zholobenko VL, Moldovan S, Hu D, Wu D, Ordonsky V V., Khodakov AY. *Nat Energy*, 2020, 5: 511–519
116. Li X, Xie J, Rao H, Wang C, Tang J. *Angew Chemie*, 2020, 132: 19870–19875
117. In S II, Nielsen MG, Vesborg PCK, Hou Y, Abrams BL, Henriksen TR, Hansen O, Chorkendorff I. *Chem Commun*, 2011, 47: 2613–2615
118. Fu C, Li F, Yang J, Xie J, Zhang Y, Sun X, Zheng X, Liu Y, Zhu J, Tang J, Gong XQ, Huang W. *ACS Catal*, 2022, 12: 6457–6463
119. Jiang Y, Zhao W, Li S, Wang S, Fan Y, Wang F, Qiu X, Zhu Y, Zhang Y, Long C, Tang Z. *J Am Chem Soc*, 2022, 144: 15977–15987
120. Graetzel M, Thampi KR, Kiwi J. *J Phys Chem*, 1989, 93: 4128–4132
121. Thampi KR, Kiwi J, Grätzel M. *Catal Letters*, 1988, 1: 109–116
122. Meng L, Chen Z, Ma Z, He S, Hou Y, Li HH, Yuan R, Huang XH, Wang X, Wang X, Long J. *Energy Environ Sci*, 2018, 11: 294–298
123. Chen X, Li Y, Pan X, Cortie D, Huang X, Yi Z. *Nat Commun*, 2016, 7: 1–8
124. Li Z, Boda MA, Pan X, Yi Z. *ACS Sustain Chem Eng*, 2019, 7: 19042–19049
125. Wang J, Hu C, Xia Y, Zhang B. *Sensors Actuators, B Chem*, 2021, 333: 129547
126. Xia Y, Wang J, Xu L, Li X, Huang S. *Sensors Actuators, B Chem*, 2020, 304: 127334
127. Chen R, Wang J, Luo S, Xiang L, Li W, Xie D. *Appl Catal B Environ*, 2020, 264: 118554
128. Liang X, Wang P, Gao Y, Huang H, Tong F, Zhang Q, Wang Z, Liu Y, Zheng Z, Dai Y, Huang B. *Appl Catal B Environ*, 2020, 260: 118151
129. Wang J, Xu R, Xia Y, Komameni S. *Ceram Int*, 2021, 47: 34437–34442
130. Yang J, Xiao W, Chi X, Lu X, Hu S, Wu Z, Tang W, Ren Z, Wang S, Yu X, Zhang L, Rusydi A, Ding J, Guo Y, Gao PX. *Appl Catal B Environ*, 2020, 265: 118469
131. Fan Y, Zhou W, Qiu X, Li H, Jiang Y, Sun Z, Han D, Niu L, Tang Z. *Nat Sustain*, 2021, 4: 509–515
132. Li X, Xie J, Rao H, Wang C, Tang J. *Angew Chemie*, 2020, 1–7
133. Miao TJ, Wang C, Xiong L, Li X, Xie J, Tang J. *ACS Catal*, 2021, 11: 8226–8238
134. Song H, Meng X, Wang S, Zhou W, Wang X, Kako T, Ye J. *J Am Chem Soc*, 2019, 141: 20507–20515
135. Zhang W, Fu C, Low J, Duan D, Ma J, Jiang W, Chen Y, Liu H, Qi Z, Long R, Yao Y, Li X, Zhang H, Liu Z, Yang J, Zou Z, Xiong Y. *Nat Commun*, 2022, 13: 1–9
136. Li W, He D, Hu G, Li X, Banerjee G, Li J, Lee SH, Dong Q, Gao T, Brudvig GW, Waegle MM, Jiang DE, Wang D. *ACS Cent Sci*, 2018, 4: 631–637
137. Song H, Meng X, Wang S, Zhou W, Song S, Kako T, Ye J. *ACS Catal*, 2020, 10: 14318–14326
138. Yang Z, Zhang Q, Ren L, Chen X, Wang D, Liu L, Ye J. *Chem Commun*, 2021
139. Hayyan M, Hashim MA, Alnashif IM. *Chem Rev*, 2016, 116: 3029–3085
140. Lien CF, Chen MT, Lin YF, Lin JL. *J Chinese Chem Soc*, 2004, 51: 37–42
141. Mayernick AD, Janik MJ. *J Catal*, 2011, 278: 16–25
142. Nishiyama H, Yamada T, Nakabayashi M, Maehara Y, Yamaguchi M, Kuromiya Y, Nagatsuma Y, Tokudome H, Akiyama S, Watanabe T, Narushima R, Okunaka S, Shibata N, Takata T, Hisatomi T, Domen K. *Nature*, 2021, 598: 304–307

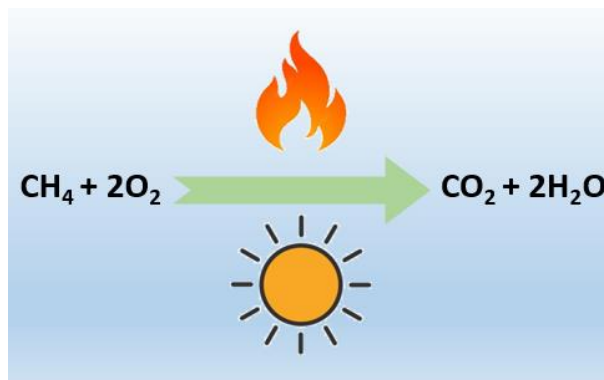


**Table of Contents graphic**